

## Highlights

### **Physics-Inspired Modeling and Content Adaptive Routing in an Infrared Gas Leak Detection Network**

Dongsheng Li, Tianli Ma, Siling Wang, Beibei Duan, Song Gao

- A physics-edge hybrid gas dynamic routing network.
- A novel edge detection operator based on adaptive gradient and phase consistency.
- A content-adaptive sparse routing path aggregation network for dynamic multi-scale feature fusion.
- Superior detection performance on the IIG and LangGas datasets, achieving consistently higher AP and AP<sub>50</sub> scores.

# Physics-Inspired Modeling and Content Adaptive Routing in an Infrared Gas Leak Detection Network

Dongsheng Li<sup>a</sup>, Tianli Ma<sup>b</sup>, Siling Wang<sup>b</sup>, Beibei Duan<sup>c</sup>, Song Gao<sup>b,\*</sup>

<sup>a</sup>*School of Mechatronic Engineering, Xi'an Technological University, Xi'an, 710021, Shaanxi, China*

<sup>b</sup>*School of Electronic Information Engineering, Xi'an Technological University, Xi'an, 710021, Shaanxi, China*

<sup>c</sup>*Shaanxi Shanhua Coal Chemical Co.,Ltd, Weinan, 714104, Shaanxi, China*

---

## Abstract

Detecting infrared gas leaks is critical for environmental monitoring and industrial safety, yet remains difficult because plumes are faint, small, semi-transparent, and have weak and diffuse boundaries. We present a physics-edge hybrid gas dynamic routing network (PEG-DRNet). First, we introduce the Gas Block, a diffusion-convection unit modeling gas transport: a local branch captures short-range variations, while a global (large-kernel) branch captures long-range propagation. An edge-gated learnable fusion module balances local detail and global context, strengthening weak-contrast plume and contour cues. Second, we propose the adaptive gradient and phase edge operator (AGPEO), computing reliable edge priors from multi-directional gradients and phase-consistent responses. These are transformed by a multi-scale edge perception module (MSEPM) into hierarchical edge features that reinforce boundaries. Finally, we propose the content-adaptive sparse routing path aggregation network (CASR-PAN). The network uses adaptive information modulation modules for fusion and self. It selectively propagates informative features across scales according to edge and content cues, enhancing cross-scale discriminability and reducing redundancy. Experiments on the IIG dataset show that PEG-DRNet achieves an overall AP of 29.8%, an AP<sub>50</sub> of 84.3%, and a small-object AP of 25.3%, surpassing the RT-DETR-R18 baseline by 3.0%, 6.5%, and 5.3%, respectively, while requiring only 43.7 Gflops and 14.9 M parameters. The proposed PEG-DRNet achieves superior

---

\*Corresponding author. Email: gaos@xatu.edu.cn

overall performance with the best balance of accuracy and computational efficiency, outperforming existing CNN and Transformer detectors in AP and AP<sub>50</sub> on the IIG and LangGas dataset.

*Keywords:* Infrared gas leak detection, Deep learning, Physics-Inspired modeling, CASR-PAN.

---

## 1. Introduction

With the rapid development of the petrochemical and natural gas industries, these sectors have provided strong support for industrialization and urbanization processes (Xu et al., 2023). However, the dense layout of industrial facilities and the extensive scale of pipeline networks have also made gas leak accidents a major concern for industrial safety and environmental protection (Lu et al., 2020). Substantial experimental evidence and accident reports indicate that gas leaks can not only directly trigger catastrophic events such as fires and explosions, but can also lead to large-scale release of toxic and hazardous substances in the early stages of leakage, thus exerting profound and long-lasting impacts on ecosystems and public health (Zuo et al., 2024; Bonvicini et al., 2015; Kopbayev et al., 2022). Therefore, achieving efficient gas leak detection has become an urgent problem that needs to be addressed.

Currently, inspection in petrochemical plants is mainly based on manual patrols, where operators carry handheld devices to check pipelines for anomalies. However, this approach requires substantial time and labor while offering low overall efficiency. To address the limitations of manual inspection, gas sensors are often deployed in industrial facilities (Wang et al., 2023). Nevertheless, such systems typically require the installation of thousands of sensors within a single area. Although these sensors can achieve gas detection to a certain extent, they are predominantly point-to-point contact-based methods that suffer from slow response, limited spatial coverage, and susceptibility to environmental interference, making them inadequate for modern industrial demands of long-range, non-contact, and highly robust monitoring.

In addition, gas leakage detection methods based on acoustic signals have gained attention due to their rapid response, non-intrusiveness, and high sensitivity, making them particularly suitable for natural gas pipeline monitoring. These methods extract acoustic signals and employ machine learning algorithms to identify leakage types without relying on complex physical

models (Quy and Kim, 2022). However, complex industrial environments are often accompanied by large amounts of redundant information, resulting in complicated and high-dimensional leakage signal data that hinder subsequent recognition. Furthermore, similar to gas sensor-based systems, acoustic methods also require the deployment of multiple acoustic sensors.

Another approach (Han et al., 2023; Shen et al., 2025) is negative pressure wave (NPW) detection, which locates leaks by analyzing the propagation characteristics of passive pressure waves induced by leakage or the reflections of active pressure waves. Compared with other methods, NPW-based detection offers advantages such as high sensitivity, short detection time, low cost, and high localization accuracy. Nevertheless, its effectiveness strongly depends on the leak location, pipeline structure, and material. In complex networks, waveforms may attenuate or distort, while environmental disturbances such as pump operation, valve actions, and flow fluctuations can easily cause false alarms or missed detections. Moreover, the method is less effective for small leaks, exhibits response delays in long-distance or large-scale networks, and entails high costs for sensor deployment and maintenance, thereby limiting its large-scale industrial applicability.

In contrast, infrared (IR) thermography enables non-contact measurement, allowing temperature distributions to be captured remotely. This feature is particularly advantageous for online monitoring in hazardous environments (Strahl et al., 2021). IR imaging can be classified into active and passive modalities. Active imaging requires an external light source, offering high sensitivity, but its safety and detectability are constrained by the external source. In gas leakage scenarios, temperature and pressure typically decrease, creating thermal differences between the leaked gas and the background, which satisfies the conditions for passive detection. Many hazardous industrial gases exhibit characteristic absorption spectra in the 3-17  $\mu\text{m}$  band. When dynamic leakage occurs within the field of view of an IR camera, radiation differences arise at the corresponding absorption wavelengths, generating grayscale contrast in the captured images. The higher the gas concentration, the stronger the absorption and the more pronounced the grayscale contrast. Furthermore, as gas plumes exhibit drifting states, plume detection and concentration estimation can be achieved through analysis of concentration differences and dynamic motion.

With the rapid advancement of deep learning, particularly convolutional neural networks (CNNs) and Transformer-based architectures, IR gas leak detection has embraced new opportunities. Deep learning has been widely

applied in image processing and object detection, where its powerful capability for automated feature extraction and representation has driven significant breakthroughs beyond traditional methods (Li et al., 2026; Zhang et al., 2025; Zhong et al., 2024; Wang et al., 2026). However, applying deep learning to IR gas leak detection still faces two critical challenges. First, gas diffusion is inherently dynamic and unstable, often exhibiting turbulence and plume-like patterns; its concentration decreases gradually from the center outward, resulting in indistinct boundaries. Moreover, thermal interactions with the environment lead to low-contrast images, while partial gas radiation overlaps with the background, making features weak and difficult to recognize accurately. Second, existing models often suffer from insufficient feature extraction capacity and high computational cost.

To address these challenges, a single-stage detection model with the following contributions is proposed. It strikes a good balance between high accuracy and computational efficiency. Figure 1 shows the comparison results of the proposed method with leading methods in terms of accuracy and computational complexity on the IIG dataset. The main contributions of this article include the following four aspects.

- A physics-inspired modeling framework for infrared gas leak detection. We introduce a Gas Block that embeds the diffusion and convection principles into the convolutional design. The proposed Gas Block explicitly models local diffusion and global convection behaviors, allowing the network to capture both fine-grained plume details and long-range contextual dependencies in a physically interpretable manner.
- An adaptive edge-aware representation mechanism. To address the weak boundaries and semi-transparent characteristics of infrared gas plumes, we propose the adaptive gradient and phase edge operator (AGPEO) and its multi-scale extension. This operator jointly encodes directional gradients and phase-consistent responses, generating reliable edge priors that enhance structural perception under low-contrast conditions.
- A content-adaptive routing strategy for efficient multi-scale fusion. We design a content-adaptive sparse routing path aggregation network (CASR-PAN) that dynamically modulates cross-scale feature propagation according to content importance. Through adaptive information modulation and importance-guided routing, the proposed mechanism enhances

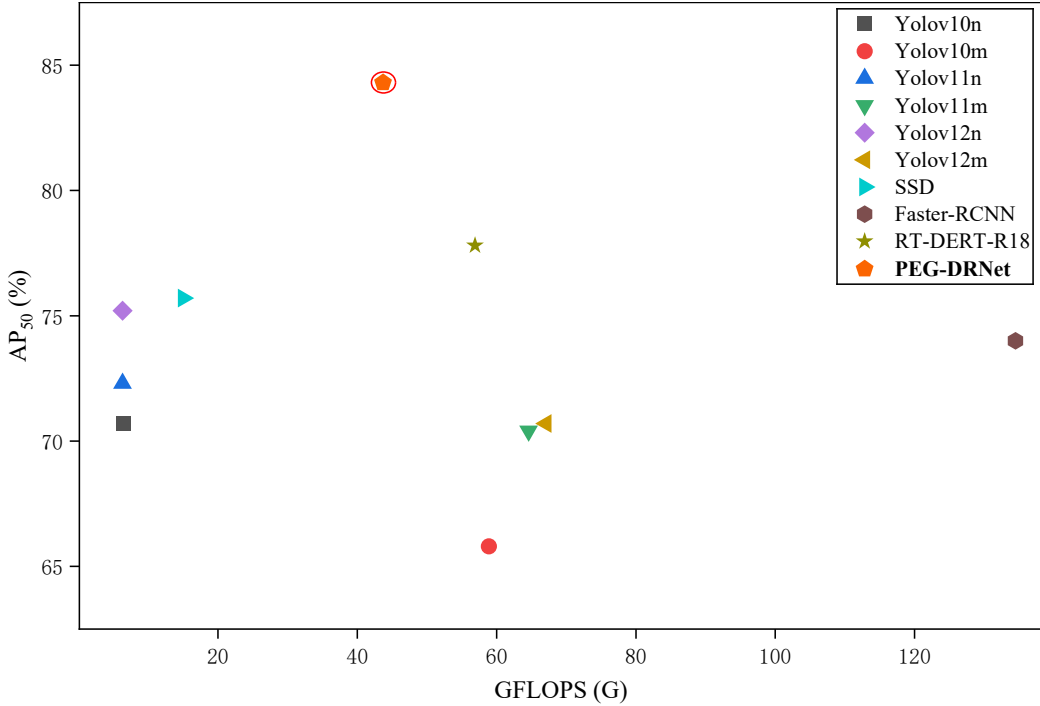


Figure 1: Comparing the AP<sub>50</sub> and Gflops of detection methods on IIG.

discriminability while significantly reducing redundant computation.

- Comprehensive validation and interpretability. We conducted extensive experiments on the IIG and LangGas datasets. PEG-DRNet achieves superior AP<sub>50</sub> performance compared with both CNN- and Transformer-based detectors. It also provides physically interpretable feature behaviors that align with real gas transport phenomena.

## 2. Related Work

### 2.1. Gas Detection

Traditional gas detection methods (Weng et al., 2024; Li et al., 2024; Qiao et al., 2022) can be broadly divided into contact-based and non-contact-based approaches. Contact-based methods mainly rely on chemical sensors (Kang et al., 2023), which directly interact with target gases and offer high sensitivity. However, their performance is easily affected by environmental factors

such as temperature, humidity, and airflow (Vergara et al., 2012). Moreover, they cannot directly localize leak sources, still requiring manual inspection.

Non-contact methods avoid direct interaction between sensors and gases, and instead infer gas presence from physical cues such as optical, acoustic, or pressure signals (Yao et al., 2024, 2025; Zhao et al., 2024). Acoustic-based solutions (e.g., ConvFormer (Li et al., 2025)) combine advanced denoising (PSOMV-VMD) with deep classification to improve low-cost leak detection, but still suffer from limited low-frequency response, domain generalization issues, and difficulties in handling complex multi-leak scenarios. Pressure-wave-based approaches (Chen et al., 2024) can achieve high sensitivity and small localization errors, yet signal attenuation, dependence on pipeline pressure, and the need for sensor arrays or openings increase deployment complexity.

With the rapid development of infrared imaging, LWIR/MWIR-based non-contact gas detection has become a key technology for industrial leak monitoring. IR cameras can visualize gas plumes at hundreds of meters, support micro-leak detection, and work under day–night conditions (Meribout, 2021). In practice, however, leak identification still largely depends on manual visual interpretation, which is costly, operator-dependent, and prone to false positives/negatives. Adverse weather, low temperature contrast, and semi-transparent plumes further reduce IR image contrast and complicate human judgment (Zimmerle et al., 2020). These limitations motivate the integration of IR imaging with robust, automated visual algorithms for precise and reliable gas leak detection.

## 2.2. *Infrared Gas Leak Detection Based on Deep Learning*

Deep learning-based infrared gas leak detection is typically built upon generic object detection frameworks, which can be categorized into two-stage and one-stage paradigms. Two-stage detectors, such as R-CNN (Girshick et al., 2014), Fast R-CNN (Girshick, 2015), and Faster R-CNN (Ren et al., 2017), employ region proposals followed by classification and bounding-box refinement, achieving high accuracy at the cost of slower inference. For example, TSFF-Net (Yao et al., 2024) fuses temporal motion and spatial details to improve SF<sub>6</sub> leak detection in complex scenes, but its reliance on motion cues and sequential computation makes static leak detection and edge deployment challenging.

One-stage detectors (e.g., YOLO and SSD (Jiang et al., 2022; Liu et al., 2016)) directly predict classes and boxes from dense feature sampling, of-

fering simpler architectures and higher speed. GasNet (Wang et al., 2020) and VideoGasNet (Wang et al., 2022) achieve stable, high-precision methane leak detection and grading in video sequences, while SRHS-Net (Pan et al., 2025) and DLFANet (Jing et al., 2025) introduce attention, multi-scale receptive fields, and lightweight backbones to enhance small vapor detection under complex backgrounds. Nevertheless, purely CNN-based detectors still struggle with faint, low-contrast plumes, are sensitive to thermal clutter, and often rely on fixed anchors and task-specific tuning, limiting generalization across environments.

To overcome the limitations of conventional CNN detectors, transformer-based models, such as DETR (Carion et al., 2020), reformulate detection as set prediction and leverage self-attention for global context modeling, removing anchors and proposal heuristics. Variants like Conditional DETR (Meng et al., 2021), DN-DETR (Li et al., 2022), and RT-DETR (Zhao et al., 2024) further improve convergence and real-time performance through hybrid encoders, denoising training, and adaptive inference. Meanwhile, in broader vision and AIGC tasks, conditional diffusion and attention-based architectures have shown strong capability in modeling fine-grained structures and complex spatial configurations for controllable generation, pose-guided synthesis, and story visualization (Shen and Tang, 2024; Shen et al., 2024, 2025), suggesting that multi-scale context modeling and physically informed priors can be beneficial for dynamic gas plume perception as well.

Beyond object detectors, edge detection and feature pyramid architectures are widely adopted to enhance small or low-contrast target representation. Classical operators such as Sobel, Canny, and Laplacian (Heath et al., 1998; Canny, 1986; Wang, 2007) emphasize intensity variations and capture structural cues, but are highly sensitive to noise, perform poorly under low contrast or semi-transparent conditions, and lack semantic awareness. Modern detectors thus integrate multi-scale feature pyramids, including FPN (Lin et al., 2017), PANet (Liu et al., 2018), BiFPN (Tan et al., 2020), and NAS-FPN (Ghiasi et al., 2019), to fuse high-level semantics with low-level details. However, their fusion strategies are typically static and content-agnostic, limiting adaptability to weak-edge or content-varying gas plumes.

To address the aforementioned limitations, we propose a physics-edge hybrid gas dynamic routing network (PEG-DRNet). The Gas Block integrates local diffusion and global convection to enhance weak-contrast plume and contour representations, while the multi-scale edge perception module (MSEPM), built upon an adaptive gradient and phase edge operator (AG-

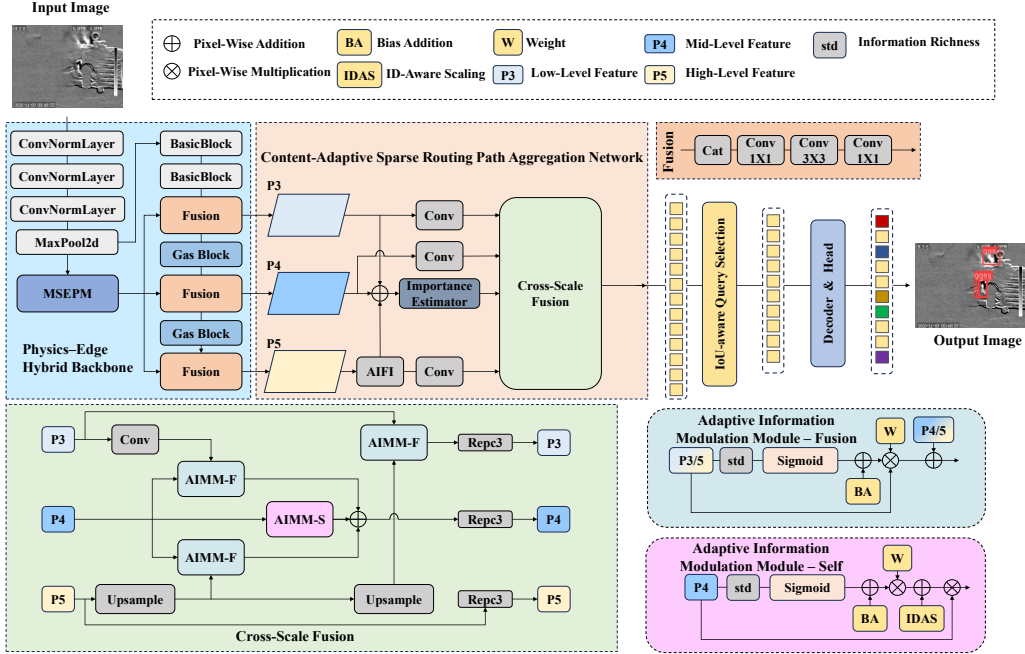


Figure 2: The overall architecture of our proposed PEG-DRNet. In AIMM-F, the bias addition (BA) represents the learned channel-wise offsets that adaptively calibrate feature responses, while in AIMM-S, the identity-aware scaling (IDAS) denotes the identity-specific scaling factors that adjust feature amplitudes based on domain knowledge. In both modules, the information richness illustrated in the figures reflects the amount of semantic and spectral information retained in the feature maps, and the weight values are generated by the Importance Estimator, indicating the relative significance of each feature channel for downstream tasks.

PEO), produces reliable edge priors under semi-transparent, low-contrast conditions. Furthermore, the content-adaptive sparse routing path aggregation network (CASR-PAN) dynamically modulates cross-scale information flow via adaptive information modulation modules for fusion(AIMM-F) and adaptive information modulation modules for self(AIMM-S), selectively propagating informative features and suppressing redundancy. This design bridges classical physics-based modeling and modern deep architectures, improving robust detection of faint and semi-transparent gas plumes under challenging industrial conditions.

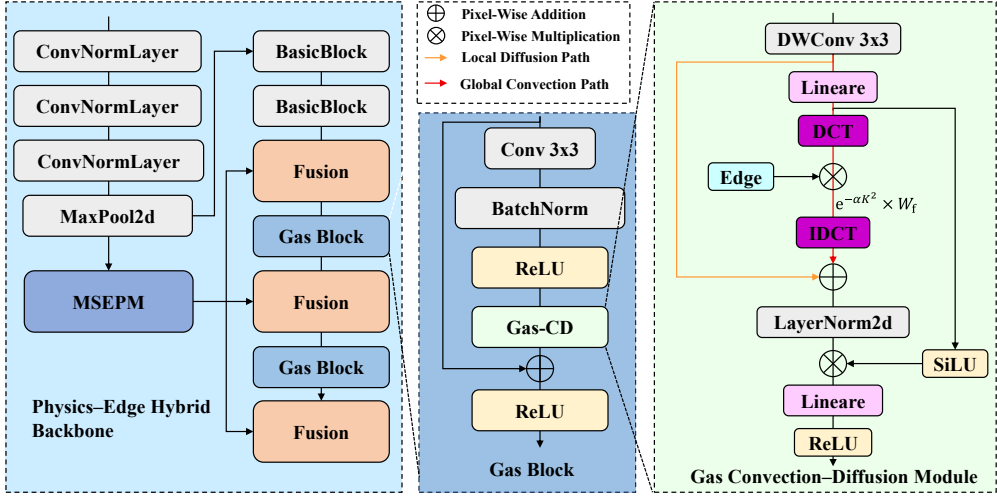


Figure 3: The Physics–Edge Hybrid Backbone integrates initial convolution and down-sampling with multiple Gas Blocks. Each Gas Block is physically inspired by the convection and diffusion equation: a local branch captures diffusion-like fine-grained features, a global branch performs frequency-domain decay to model convection-like transport, and edge-aware gating modulates global features, with residual fusion producing the final output.

### 3. Methodology

#### 3.1. Overview Of The Gas Leak Detection Framework

The proposed PEG-DRNet, built upon the RT-DETR framework, integrates physics-inspired modeling, edge-aware enhancement, and adaptive multi-scale fusion for robust infrared gas leak detection, as illustrated in Figure 2. In the Physics–Edge Hybrid Backbone, the proposed Gas Block models the dual physical behaviors of gas diffusion and convection through local and global branches. The local diffusion branch captures fine-grained textures and weak boundaries essential for small and faint plumes, while the frequency-domain global convection branch aggregates long-range contextual information to preserve plume integrity. An edge-gated fusion mechanism adaptively balances these cues, improving plume visibility under low-contrast conditions. To provide reliable boundary guidance, the multi-scale edge perception module (MSEPM) employs an adaptive gradient and phase edge operator (AGPEO) to extract directional gradient and phase features and construct hierarchical edge maps across multiple scales. The structure of the

Physics-Edge Hybrid Backbone is illustrated in Figure 3. Before entering the neck, an attention-based intra-scale feature interaction (AIFI) module enhances semantic consistency and fuses these edge-aware multi-scale features. Finally, the content-adaptive sparse routing path aggregation network (CASR-PAN), guided by an importance estimator (IE), dynamically propagates informative paths while suppressing redundant ones. CASR-PAN integrates adaptive information modulation modules for fusion (AIMM-F) and for self (AIMM-S), with their fusion weights derived from the IE, to adaptively control cross-scale feature propagation and intra-scale enhancement. This design enables efficient and discriminative multi-scale aggregation, selectively amplifying salient features and improving overall detection performance. Collectively, these modules allow PEG-DRNet to achieve accurate and interpretable detection of weak and semi-transparent gas plumes.

### 3.2. Gas Block

The proposed Gas Block is inspired by the physical transport of gases in a medium, which is governed by the convection and diffusion equation:

$$\frac{\partial u(x, y, t)}{\partial t} = D \nabla^2 u(x, y, t) - \mathbf{v} \cdot \nabla u(x, y, t), \quad (1)$$

where  $u(x, y, t)$  denotes the gas concentration at spatial location  $(x, y)$  and time  $t$ ,  $D$  is the diffusion coefficient, and  $\mathbf{v} = (v_x, v_y)$  represents the velocity field. The Laplacian operator:

$$\nabla^2 u = \frac{\partial^2 u}{\partial x^2} + \frac{\partial^2 u}{\partial y^2}, \quad (2)$$

quantifies local diffusion, which acts isotropically over a small spatial neighborhood, smoothing high-frequency variations. Consequently, diffusion naturally corresponds to local feature propagation within the network. In contrast, the convection term:

$$\mathbf{v} \cdot \nabla u = v_x \frac{\partial u}{\partial x} + v_y \frac{\partial u}{\partial y}. \quad (3)$$

represents directional transport along the velocity field, potentially over long spatial distances, corresponding to global feature propagation. Expanding the equation explicitly separates these contributions:

$$\frac{\partial u(x, y, t)}{\partial t} = D \left( \frac{\partial^2 u}{\partial x^2} + \frac{\partial^2 u}{\partial y^2} \right) - v_x \frac{\partial u}{\partial x} - v_y \frac{\partial u}{\partial y}. \quad (4)$$

The analytical solution in the frequency domain is given by:

$$\tilde{u}(k_x, k_y, t) = \tilde{u}(k_x, k_y, 0) \exp \left\{ -D(k_x^2 + k_y^2)t - i(v_x k_x + v_y k_y)t \right\}, \quad (5)$$

where  $\tilde{u}(k_x, k_y, t)$  denotes the Fourier transform of  $u(x, y, t)$ ,  $(k_x, k_y)$  are spatial frequency components, and  $i$  is the imaginary unit. The first term in the exponent,  $-D(k_x^2 + k_y^2)t$ , represents diffusion-induced attenuation of high-frequency components, whereas the second term,  $-i(v_x k_x + v_y k_y)t$ , corresponds to a phase shift encoding directional convection. The spatial solution is obtained via inverse Fourier transform:

$$u(x, y, t) = \mathcal{F}^{-1} \left\{ \tilde{u}(k_x, k_y, 0) \exp[-D(k_x^2 + k_y^2)t - i(v_x k_x + v_y k_y)t] \right\}. \quad (6)$$

This formulation indicates that the initial gas concentration field undergoes local diffusion and directional convection simultaneously, which directly motivates the design of the Gas Block.

Although diffusion is governed by the Laplacian operator, it is important to note that a learnable depthwise convolution does not strictly correspond to a discrete Laplacian. The classical five-point stencil of the Laplacian enforces a fixed second-order finite-difference pattern, whereas a depthwise convolution kernel is freely learned and therefore not guaranteed to exhibit second-order behavior unless explicitly initialized or regularized toward such a structure. Thus, the local branch should be interpreted as a data-driven approximation of diffusion that can express Laplacian-like smoothing but is not mathematically equivalent to  $\nabla^2 u$ . The network employs a physically inspired but flexible formulation that allows local propagation to adapt to data characteristics.

In the network, the diffusion-like local branch approximates the Laplacian operator using depthwise convolution:

$$X_{\text{local}} = \text{DWConv}(X), \quad (7)$$

followed by linear projection and splitting into a feature component and a gating vector:

$$X_{\text{proj}}, Z = \text{split}(\text{Linear}(X_{\text{local}}), 2), \quad (8)$$

allowing adaptive channel-wise modulation that captures multi-scale local smoothing.

The frequency-domain decay term  $e^{-\alpha K^2}$  in the global branch is motivated by the Fourier-domain solution of the diffusion equation, which attenuates

high-frequency components as  $e^{-D(k_x^2+k_y^2)t}$ . Since the discrete cosine transform (DCT) provides a real-valued basis related to the Fourier cosine basis, applying  $e^{-\alpha K^2}$  yields a practical approximation to diffusion-driven smoothing. However, this equivalence is approximate due to differing boundary conditions, discretization effects, and the absence of complex phase terms. Consequently,  $\alpha$  should be regarded as a learnable surrogate for the diffusion scale  $Dt$ , enabling physically inspired frequency-selective smoothing while remaining data-adaptive.

The global branch, inspired by convection, operates in the frequency domain. The projected features are transformed via discrete cosine transform (DCT) and modulated by a learnable frequency decay kernel:

$$X_{\text{dct}}^{\text{decay}} = \text{DCT}(X_{\text{proj}})e^{-\alpha K^2}W_f, \quad (9)$$

where  $K^2 = \omega_x^2 + \omega_y^2$ ,  $\omega_x = \pi k_x/W$ ,  $\omega_y = \pi k_y/H$ ,  $\alpha$  is a learnable decay coefficient, and  $W_f$  is a channel-wise weight vector. The inverse DCT reconstructs the global feature:

$$X_{\text{global}} = \text{IDCT}(X_{\text{dct}}^{\text{decay}}), \quad (10)$$

propagating information over long spatial distances while preserving global context.

While diffusion corresponds to magnitude attenuation, convection introduces a frequency-domain phase shift  $\exp[-i(v_x k_x + v_y k_y)t]$  that represents directional transport. Because the DCT basis is real-valued and does not capture complex phase modulation, the proposed global branch does not explicitly implement this phase behavior. Instead, directional transport is approximated implicitly through global DCT-based propagation combined with the edge-aware modulation mechanism, allowing the model to learn data-driven feature displacement patterns that serve as a practical surrogate for advective transport in feature space.

To enhance sensitivity to weak infrared gas boundaries, an edge-aware gating mechanism is employed. Given an edge prior  $E$ , the gating map is computed as:

$$G_{\text{edge}}(E) = \sigma(\text{Conv}_{1 \times 1}(E)), \quad (11)$$

which modulates the global features:

$$X_{\text{global}} \leftarrow X_{\text{global}} G_{\text{edge}}(E). \quad (12)$$

Finally, local and global features are fused, normalized, and modulated by the gating vector  $Z$  before projection back to the original feature dimension:

$$\begin{aligned} Y' &= \text{OutLinear}\left(\text{OutNorm}(X_{\text{local}} + X_{\text{global}})\sigma(Z)\right), \\ Y &= \text{Act}(Y' + X_{\text{res}}). \end{aligned} \quad (13)$$

where  $X_{\text{local}}$  and  $X_{\text{global}}$  denote the local and global feature branches,  $Z$  is the gating vector, and  $X_{\text{res}}$  is the residual input.

By explicitly decomposing feature transformation into diffusion-like local smoothing and convection-inspired global transport, the Gas Block establishes a physically interpretable and dynamically adaptive mechanism. The local branch captures fine-grained details, while the global branch facilitates long-range feature propagation, ensuring robust and accurate infrared gas detection.

### 3.3. Multi-Scale Edge Perception Module

In infrared gas imaging scenarios, gas targets typically exhibit transparent or semi-transparent characteristics, and the temperature difference between the targets and the background is often minimal, resulting in extremely weak edge gradient signals. Convolutional neural networks respond poorly to such weak-gradient targets and are prone to misidentifying background heat sources or complex textures as valid edges, which severely degrades subsequent detection accuracy.

To address this issue, the multi-scale edge perception module (MSEPM), which combines multi-directional gradient detection with phase consistency analysis to preserve subtle gas edge information while effectively suppressing background noise, is introduced. Specifically, the module first employs the adaptive gradient and phase edge operator (AGPEO) to adaptively fuse gradient and phase information, enhancing the edge representation of gas targets. Subsequently, multi-scale pooling and feature transformation are applied to generate edge feature maps corresponding to the shallow, middle, and deep layers of the backbone network, providing more discriminative edge representations for subsequent feature fusion and target detection. The module architecture is illustrated in Figure 4.

Given an input feature map  $X \in \mathbb{R}^{C \times H \times W}$ , the AGPEO first applies directional convolution kernels along four orientations  $\{0^\circ, 45^\circ, 90^\circ, 135^\circ\}$  to extract gradient responses. The gradient feature is defined as:

$$G(x, y) = \max_{\theta \in \{0^\circ, 45^\circ, 90^\circ, 135^\circ\}} |K_\theta * X(x, y)|, \quad (14)$$

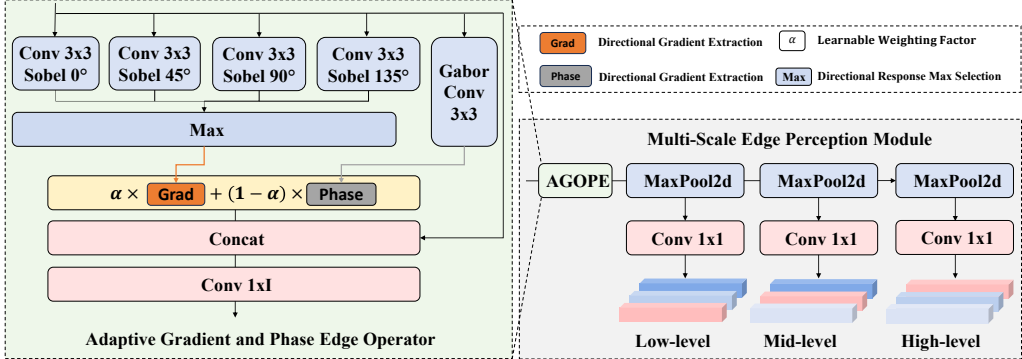


Figure 4: Architecture of the multi-scale edge perception module (MSEPM) and adaptive gradient and phase edge operator (AGPEO)

where  $K_\theta$  denotes the convolution kernel along direction  $\theta$ , and  $*$  represents the convolution operation, and  $x, y$  denote the spatial coordinates within the feature map. The maximum absolute response across the four orientations is taken as the gradient feature.

To further capture the structural consistency of weak edges, phase congruency is computed as:

$$P(x, y) = \frac{\sum_s A_s(x, y) \cos(\phi_s(x, y) - \phi(x, y))}{\sum_s A_s(x, y) + \varepsilon}, \quad (15)$$

where  $A_s(x, y)$  and  $\phi_s(x, y)$  denote the amplitude and phase at scale  $s$ ,  $\phi(x, y)$  is the mean phase, and  $\varepsilon$  is a small constant to avoid division by zero.

Finally, the gradient and phase features are adaptively fused using a learnable weighting factor  $\alpha \in [0, 1]$ :

$$E_0(x, y) = \alpha G(x, y) + (1 - \alpha) P(x, y). \quad (16)$$

where  $E_0$  denotes the initial edge feature map, which retains weak gas boundaries while suppressing background noise. The fusion weight  $\alpha$  is implemented as a learnable scalar parameter and optimized jointly with the network via back-propagation under the detection loss. This design enables adaptive balancing between gradient-based and phase-based cues in a data-driven manner, without introducing additional supervision or manual tuning.

Based on the initial edge feature map  $E_0$  obtained by the adaptive gradient and phase edge operator (AGPEO), the multi-scale edge perception module (MSEPM) is designed to construct hierarchical edge representations

aligned with different backbone stages. Specifically,  $E_0$  is progressively down-sampling by a  $2 \times 2$  max-pooling operator to generate multi-scale edge features:

$$E_i = \text{Pool}(E_{i-1}), \quad i = 1, 2, \dots, N, \quad (17)$$

where  $\text{Pool}(\cdot)$  denotes the max-pooling operation, and  $N$  is the number of scales. Each scale-specific edge feature is then transformed by a  $1 \times 1$  convolution to adjust the channel dimensions:

$$\hat{E}_i = \text{Conv}_{1 \times 1}(E_i), \quad i = 0, 1, \dots, N. \quad (18)$$

Finally, the set of transformed features  $\{\hat{E}_0, \hat{E}_1, \dots, \hat{E}_N\}$  corresponds to the shallow, middle, and high-level edge features, which are fed into the subsequent backbone and neck for enhanced feature fusion. In this way, the multi-scale edge perception module (MSEPM) provides more discriminative edge representations, enabling reliable detection of weak and transparent gas targets in complex infrared imaging scenarios.

### 3.4. Content-Adaptive Sparse Route Path Aggregation Network

Traditional FPN and PAN architectures employ fixed top-down and bottom-up pathways for feature fusion, in which fusion weights are static and implemented via simple addition or concatenation. Although BiFPN introduces learnable weights, they remain constrained by rigid structures, while NAS-FPN constructs predetermined or NAS-searched cross-scale connections without true content adaptivity.

In contrast, the proposed content-adaptive sparse routing path aggregation network (CASR-PAN) performs fully content-driven multi-scale fusion. As illustrated in Figure 2, CASR-PAN dynamically generates spatially varying path weights through an importance estimator (IE), selectively enhancing or suppressing cross-scale feature flows using sparse routing. Multi-path outputs at the same scale are further consolidated by RepC3 modules, achieving stable gradient propagation and discriminative multi-scale representation. The internal structure of the IE is shown in Figure 5.

For the content-adaptive sparse route path aggregation network (CASR-PAN), the importance estimator (IE) computes an importance map  $\mathbf{I} \in \mathbb{R}^{B \times C \times H \times W}$  for an input feature  $\mathbf{X} \in \mathbb{R}^{B \times C \times H \times W}$  as:

$$\mathbf{I} = \sigma(w_g \cdot \tilde{\mathbf{G}} + w_l \cdot \mathbf{L} + w_d \cdot \mathbf{D}), \quad (19)$$

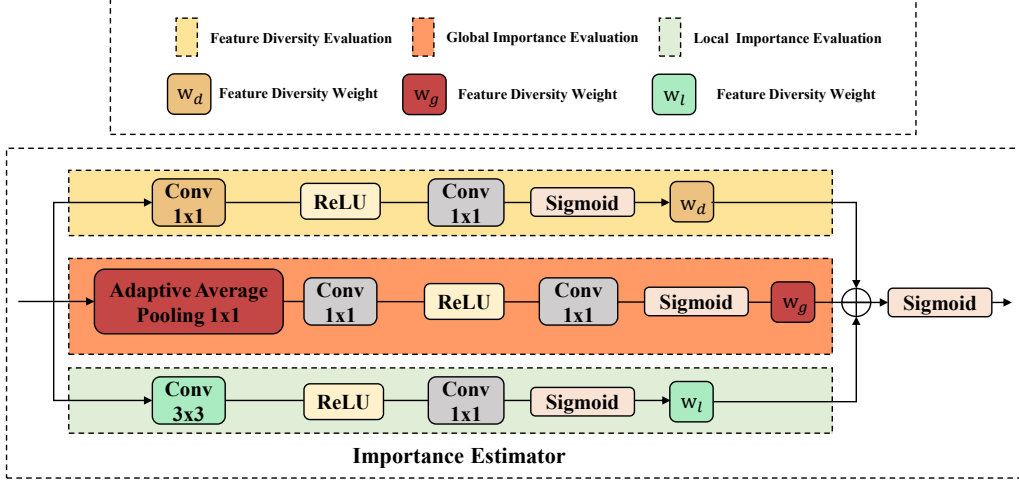


Figure 5: Architecture of the importance estimator.

where  $\sigma(\cdot)$  denotes the element-wise sigmoid function ensuring the importance values lie in  $[0, 1]$ , and  $w_g, w_l, w_d$  are learnable fusion weights normalized via softmax.

The three components  $\tilde{\mathbf{G}}$ ,  $\mathbf{L}$ , and  $\mathbf{D}$  are designed to capture complementary aspects of feature importance. Specifically,  $\tilde{\mathbf{G}}$  represents the global importance. It is obtained by applying global average pooling to  $\mathbf{X}$ , followed by a  $1 \times 1$  convolution, ReLU activation, another  $1 \times 1$  convolution with sigmoid, and upsampling to the original spatial resolution. The global average pooling aggregates information across all spatial locations, producing a vector that represents the overall contribution of each channel to the feature map, independent of spatial position. The subsequent  $1 \times 1$  convolutions allow non-linear interactions between channels, enhancing the representation of channels that are globally significant. This combination effectively captures holistic, channel-wise importance, which is why it serves as a “global” measure: it summarizes each channel’s overall influence rather than local variations. The local importance  $\mathbf{L}$  is computed using a  $3 \times 3$  convolution followed by ReLU, a  $1 \times 1$  convolution, and sigmoid activation. A  $3 \times 3$  convolution operates on a small neighborhood of each spatial location, naturally focusing on local spatial dependencies. By scanning the feature map with a limited receptive field, it captures fine-grained variations, such as edges, textures, or localized patterns, that may not be reflected in global pooling.

This design ensures that the estimator can adaptively weigh spatially local features, distinguishing important regions from surrounding areas. The following  $1 \times 1$  convolution allows channel-wise integration while maintaining spatial resolution. The diversity component  $\mathbf{D}$  estimates feature diversity via  $1 \times 1$  convolutions followed by ReLU and another  $1 \times 1$  convolution with sigmoid, further modulated by the per-channel standard deviation of  $\mathbf{X}$ . Where,  $1 \times 1$  convolutions operate independently at each spatial location, focusing solely on cross-channel interactions. Combined with the statistical measure of variation, this highlights channels that carry complementary or non-redundant information. The use of  $1 \times 1$  convolutions ensures that diversity is measured across channels rather than across space, emphasizing the variety and richness of feature representations rather than spatial structure. By combining these global, local, and diversity cues, with carefully chosen operations that align with their conceptual goals, the IE effectively produces a content-adaptive importance map that guides the sparse route path aggregation in CASR-PAN, enabling the network to prioritize informative features while suppressing less relevant ones.

Based on  $\mathbf{I}$ , a  $1 \times 1$  convolution layer transforms the aggregated importance map into four path weights:

$$[\mathbf{W}_1, \mathbf{W}_2, \mathbf{W}_3, \mathbf{W}_4] = \sigma(\text{Conv}_{1 \times 1}(\mathbf{I})), \quad (20)$$

These four routing weights are subsequently used to guide the cross-scale feature fusion process.

Guided by  $\mathbf{W}$  path weights, the adaptive information modulation module-fusion (AIMM-F) fuses two features  $\mathbf{F}_1, \mathbf{F}_2 \in \mathbb{R}^{B \times C \times H \times W}$ :

$$\mathbf{Y} = \mathbf{F}_1 + \mathbf{F}_2(\mathbf{W}(BA + \sigma(\text{std}(\mathbf{F}_2)))) \quad (21)$$

while the adaptive information modulation module-self (AIMM-S) adjusts a single feature  $\mathbf{F}$ :

$$\mathbf{Y} = \mathbf{F}(IDAS + \mathbf{W}(BA + \sigma(\text{std}(\mathbf{F})))) \quad (22)$$

where  $\mathbf{W}$  denotes the learned routing weight, and  $\text{std}(\cdot)$  measures channel-wise information richness. In AIMM-F, a bias addition term BA is introduced to the content-driven modulation to establish a non-zero lower bound for feature contribution. In practice, BA is fixed to 0.5, which prevents moderately

informative regions from being excessively suppressed during adaptive fusion and improves numerical stability across different feature scales. Rather than being learned, this fixed bias regularizes the modulation strength and ensures consistent behavior across layers. In AIMM-S, identity-aware scaling (IDAS) is enforced by setting IDAS = 1, which explicitly preserves an identity mapping of the original feature. Adaptive modulation is applied in a residual multiplicative manner, allowing selective amplification guided by routing weights while maintaining the original feature magnitude. This design avoids feature distortion or collapse and ensures that self-enhancement strengthens discriminative regions without nullifying existing information. Together, BA and IDAS provide complementary stabilization mechanisms: BA controls the minimum contribution in cross-level fusion, while IDAS preserves feature integrity in self-enhancement. As a result, CASR-PAN achieves content-adaptive amplification of discriminative features while maintaining stable optimization and consistent feature semantics.

CASR-PAN constructs three explicit cross-scale pathways (high-to-mid, high-to-low, low-to-mid) and one self-enhancement path. Routed features are aggregated and refined through RepC3 modules and subsequently fed into the RT-DETR decoder.

Although CASR-PAN is implemented through the content-driven importance estimator (IE) and the AIMM-F/AIMM-S modules, its behavior can be interpreted from a physics-inspired perspective that complements, rather than replaces, the content-adaptive mechanism. The routing weights are still predicted entirely from feature content, but their functional role resembles a spatially varying transport strength analogous to convection in physical systems. Let  $\{F_s\}$  denote the feature maps from different pyramid levels. At a given spatial location  $(x, y)$ , the AIMM-F and AIMM-S modules receive:

- $F_{\text{local}}(x, y)$ : the feature from the current scale.
- $F_{\text{transport}}(x, y)$ : the feature transported from another scale through a cross-scale path (e.g., P5→P4, P3→P4).
- $W(x, y)$ : the routing weight predicted by the IE and the  $1 \times 1$  convolution, subsequently normalized by a sigmoid. This weight lies in  $[0, 1]$  and reflects the local content importance for cross-scale propagation.

The output of AIMM-F/AIMM-S at location  $(x, y)$  can be written as:

$$F_{\text{out}}(x, y) = (1 - W(x, y)) F_{\text{local}}(x, y) + W(x, y) F_{\text{transport}}(x, y), \quad (23)$$

a convex combination controlled by the content-adaptive routing weight. Equation (23) represents how much information is retained from the current scale versus transported from neighboring scales.

The structure of Eq. (23) mirrors the explicit discretization of the convection operator:

$$u^{t+1} = u^t - \Delta t \mathbf{v} \cdot \nabla u, \quad (24)$$

where  $\|\mathbf{v}(x, y)\|\Delta t$  determines how strongly information flows along the convection direction.

By analogy, the content-derived routing weight satisfies:

$$W(x, y) \approx \|\mathbf{v}(x, y)\|\Delta t. \quad (25)$$

indicating that CASR-PAN implicitly learns a spatially varying “velocity magnitude” that governs cross-scale feature transport. Crucially, unlike physical velocity fields, this “velocity” is not predefined but emerges entirely from the image content through the IE, making the routing mechanism both content-aware and physically interpretable.

Large values of  $W(x, y)$  promote long-range feature transport from other pyramid levels, particularly helpful in smooth, low-gradient gas plume regions. Small values retain  $F_{\text{local}}(x, y)$ , preserving boundaries and high-frequency structures. Thus, the Gas Block models convection–diffusion behavior within a scale, while CASR-PAN applies a convection-inspired transport mechanism across scales, jointly forming a unified physics-consistent multi-level propagation framework.

## 4. Experiment And Analysis

### 4.1. Dataset

Experiments were carried out on two benchmark infrared gas leakage datasets. The IIG dataset, proposed by Yu et al. (Yu et al., 2024), was acquired at Zhejiang University using a VF 330-1000 handheld thermal infrared imaging device and contains a total of 11,186 annotated gas leakage instances. In accordance with the dataset protocol, the images were partitioned into training and testing subsets at a ratio of 4:1, resulting in 4,453 training images with 9,289 instances and 1,116 testing images with 1,897 instances. In addition, the LangGas dataset (Guo et al., 2025) was utilized to assess the generalization capability of the proposed approach. LangGas is a

synthetically generated infrared gas leakage dataset constructed by compositing physically realistic gas plumes and various interfering foreground objects onto diverse background scenes. Although the dataset provides pixel-level segmentation annotations and video sequences, we manually labeled the images for object detection tasks. The annotated data were divided into 1,289 training images and 323 validation images.

#### 4.2. Training Environment And Detailed Settings

To ensure reproducibility and rigorous evaluation, all experiments were conducted under consistent conditions. The system is equipped with an AMD Ryzen 7 9700X CPU and an NVIDIA GeForce RTX 5070 Ti GPU with 16 GB of memory. The software environment includes Python 3.10.16, PyTorch 2.5.1, and CUDA 12.4. Input images were uniformly resized to  $640 \times 640$ , and training was performed for 200 epochs with a batch size of 4. The AdamW optimizer was used with an initial learning rate of 0.0001 and a momentum of 0.9. To ensure a fair evaluation of various gas leak detection methods, we conducted a comprehensive assessment of model performance. The computational complexity of the network architecture is measured in terms of time complexity (Gflops) and space complexity (Params). Following the COCO evaluation protocol (Lin et al., 2014), we use the RT-DETR network model as a baseline.

#### 4.3. Comparative Experiments

To evaluate the effectiveness of the proposed PEG-DRNet, several representative object detection algorithms, including YOLOv10 (Wang et al., 2024), YOLOv11 (Khanam and Hussain, 2024), YOLOv12 (Tian et al., 2025), SSD (Liu et al., 2016), Faster R-CNN (Ren et al., , 2017), and RT-DETR (Zhao et al., 2024), were selected as baselines for comparison. The quantitative results are summarized in Table 1, highlighting the performance advantages of PEG-DRNet over these existing methods.

Our model achieves the highest AP of 29.8%, outperforming all baselines (e.g., +3.0% over RT-DETR-R18 and +3.6% over Yolov10n), which demonstrates the benefits of integrating Physics-Inspired modeling, edge-aware representation, and adaptive multiscale fusion. Notably, PEG-DRNet attains a substantial improvement in small-object detection ( $AP_S=25.3\%$ , +5.3% over Yolov12n), indicating that fine-grained spatial details are well preserved,

Table 1: Comparison of detection performance between the proposed method and mainstream models on the IIG dataset.

Model	AP (%)	AP <sub>50</sub> (%)	AP <sub>75</sub> (%)	AP <sub>S</sub> (%)	AP <sub>M</sub> (%)	AP <sub>L</sub> (%)	Gflops (G)	Params (M)
Yolov10n (Wang et al., 2024)	27.0	70.7	<b>10.6</b>	17.6	<b>34.6</b>	38.4	6.5	2.265
Yolov10m	25.2	65.8	11.2	14.8	34.2	23.6	58.9	15.313
Yolov11n (Khanam and Hussain, 2024)	24.7	72.3	6.7	16.7	31.1	<b>42.8</b>	<b>6.3</b>	2.582
Yolov11m	25.8	70.4	10.4	14.7	34.5	31.5	67.6	20.030
Yolov12n (Tian et al., 2025)	25.7	75.2	7.2	19.0	30.9	29.2	<b>6.3</b>	<b>2.555</b>
Yolov12m	25.2	70.7	9.8	18.2	33.3	12.7	67.1	20.105
SSD (Liu et al., 2016)	24.8	75.7	6.5	20.7	29.0	23.3	15.03	13.06
Faster-RCNN (Ren et al., , 2017)	26.2	74.0	9.6	18.1	33.7	24.0	134.491	41.352
RT-DETR-R18 (Zhao et al., 2024)	26.8	77.8	8.7	19.9	32.0	37.1	56.9	19.873
PEG-DRNet	<b>29.8</b>	<b>84.3</b>	8.5	<b>25.3</b>	32.5	42.6	43.7	14.932

Table 2: Comparison of detection performance between the proposed method and mainstream models on the LangGas dataset.

Model	AP (%)	AP <sub>50</sub> (%)	AP <sub>75</sub> (%)	AP <sub>S</sub> (%)	AP <sub>M</sub> (%)	AP <sub>L</sub> (%)	Gflops (G)	Params (M)
Yolov10n (Wang et al., 2024)	32.3	61.7	30.2	0.1	11.4	39.8	6.5	2.265
Yolov10m	28.8	56.9	26.8	0.8	14.1	34.9	58.9	15.313
Yolov11n (Khanam and Hussain, 2024)	33.5	65.1	30.1	1.7	14.7	40.5	<b>6.3</b>	2.582
Yolov11m	32.6	65.1	28.1	1.6	14.5	39.8	67.6	20.030
Yolov12n (Tian et al., 2025)	34.4	65.7	31.0	1.1	15.3	41.3	<b>6.3</b>	<b>2.555</b>
Yolov12m	32.8	63.6	28.7	1.7	13.8	39.7	67.1	20.105
SSD (Liu et al., 2016)	30.7	64.8	25.3	1.9	11.2	37.6	15.03	13.06
Faster-RCNN (Ren et al., , 2017)	30.3	62.1	24.0	1.1	10.7	38.1	134.491	41.352
RT-DETR-R18 (Zhao et al., 2024)	31.4	63.6	28.4	2.6	12.0	38.6	56.9	19.873
PEG-DRNet	<b>36.3</b>	<b>68.5</b>	<b>31.2</b>	<b>3.7</b>	<b>15.4</b>	<b>43.9</b>	43.7	14.932

while medium- and large-object detection ( $AP_M=32.5\%$ ,  $AP_L=42.6\%$ ) remains competitive, highlighting balanced scale adaptability. Despite superior accuracy, the model requires only 43.7 Gflops and 14.932M parameters, lower than heavier baselines such as Faster-RCNN (134.5 Gflops, 41.35M), demonstrating practical deployability. The high  $AP_{50}=84.3\%$  confirms reliable region-level detection, whereas the comparatively lower  $AP_{75}$  reflects the intrinsic difficulty of precise bounding-box alignment for diffuse and semi-transparent gas plumes in infrared imagery, where ambiguous boundaries, and background clutter limit high-IoU localization; addressing such fine-grained localization remains a challenging direction for future work.

To ensure the robustness and generalizability of the proposed framework, we further evaluate PEG-DRNet on the LangGas dataset. As a complementary benchmark to the IIG dataset. Consistent with the observations reported earlier on the IIG benchmark, PEG-DRNet again delivers the strongest overall performance (Table 2). Specifically, it achieves an AP of 36.3%, outperforming all YOLO-based methods and the transformer-driven RT-DETR-R18. The gains remain evident across  $AP_{50}$ ,  $AP_{75}$ , and scale-specific metrics, confirming that the physics-inspired design yields benefits beyond a single domain.

To further validate the effectiveness of the proposed method, a visualization comparison experiment was conducted. The YOLO series employed the YOLOv12n, which currently achieves the best detection performance among its variants. The comparative visualization results are presented in Figure 6. Although YOLOv12 has relatively fewer parameters and lower computational complexity, the visualization comparison reveals that it suffers from a high false negative rate (FNR), which is a critical issue in gas leak detection tasks. The single-stage detector SSD exhibits similar shortcomings, indicating its limited sensitivity to faint and small gas plumes. In contrast, Faster R-CNN achieves higher detection accuracy than the previous two models; however, its heavy model parameters and substantial computational burden hinder deployment on resource-constrained edge devices. The RT-DETR-R18 model offers a better trade-off between detection accuracy and computational efficiency, yet it still exhibits false positives and missed detections under challenging conditions. In comparison, the proposed PEG-DRNet demonstrates superior localization capability and successfully identifies most gas plumes, outperforming the mainstream detection models. Nevertheless, it still struggles with extremely small and visually indistinct gas leaks at long distances. Through comprehensive analysis of these scenarios, it is concluded that gas detection accuracy decreases in visually complex and cluttered backgrounds compared with simple and uniform scenes. Moreover, scenes containing larger and more structured gas plumes tend to yield higher detection accuracy. Future research will focus on enhancing the detection precision of subtle and blurry gas leaks under complex backgrounds, which is expected to further advance the development of vision-based infrared gas detection systems.

#### 4.4. Ablation Experiments

Table 3: Ablation experiments of the backbone. Adaptive gradient and phase edge operator (AGPEO) denotes the proposed adaptive gradient–phase operator that forms the core of the multi-scale edge perception module(MSEPM).  $\times$  indicates the module is not used,  $\checkmark$  indicates the module is used.

Gas Block	AGPEO	AP	AP <sub>50</sub>	AP <sub>S</sub>	AP <sub>M</sub>	AP <sub>L</sub>	Gflops (G)	Params (M)
$\times$	$\times$	26.8	77.8	19.9	32.0	37.1	56.9	19.873
$\checkmark$	$\times$	28.5	80.7	22.2	32.8	37.3	<b>51.9</b>	<b>16.620</b>
$\times$	$\checkmark$	27.9	80.4	24.0	30.6	38.1	59.8	21.119
$\checkmark$	$\checkmark$	<b>29.5</b>	<b>81.0</b>	<b>24.3</b>	<b>33.5</b>	<b>38.9</b>	54.8	17.866

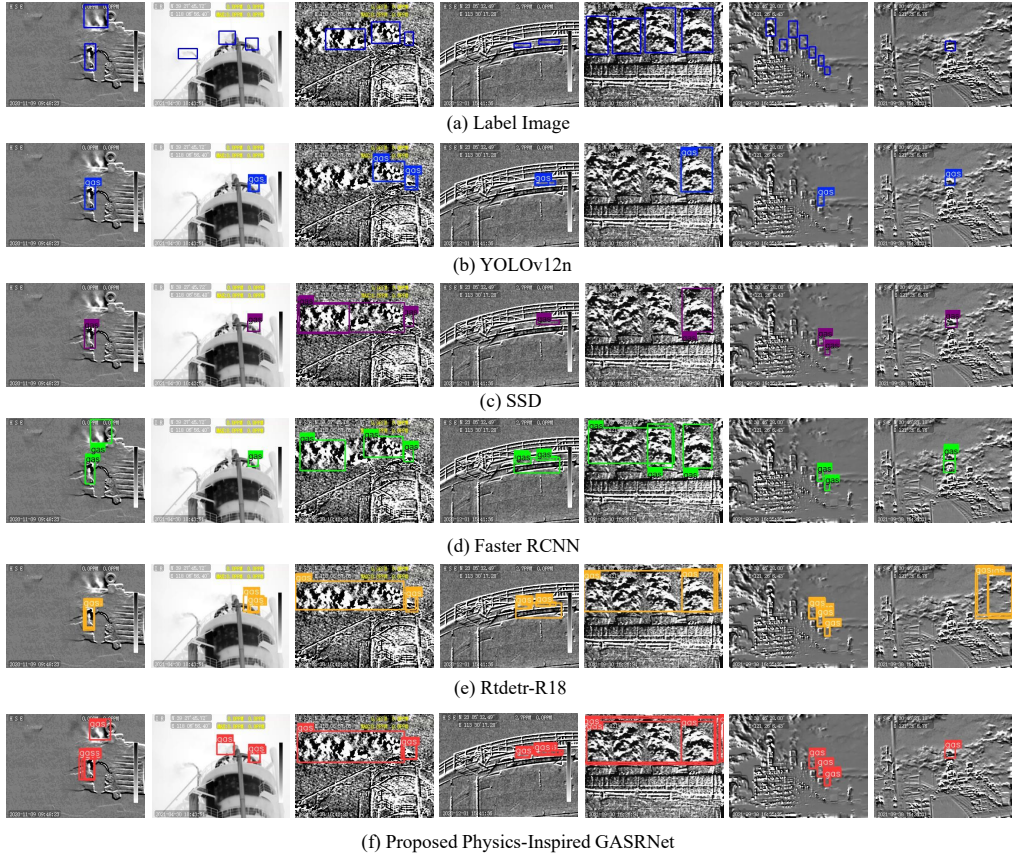


Figure 6: Visualization comparison of different detectors on the IIG dataset. Each row represents the detection results obtained by a specific model. The proposed PEG-DRNet achieves more accurate gas boundary localization and superior plume completeness compared with other methods.

To evaluate the effectiveness of the proposed Physics–Edge Hybrid Backbone, we conducted ablation experiments by progressively incorporating the Gas Block and the proposed AGPEO-based edge perception module into the ResNet18 baseline. The results are summarized in Table 3. The baseline ResNet18 achieves an overall AP of 26.8%, serving as the reference. Introducing the AGPEO module individually increases AP to 27.9% (+1.1), accompanied by clear improvements in  $AP_{50}$ . This performance gain can be attributed to AGPEO’s adaptive gradient–phase fusion and multi-scale edge perception, which selectively amplify subtle edge signals from weak or semi-transparent gas targets while suppressing background noise. Integrating the Gas Block alone results in an overall AP of 28.5%, with notable improvements in medium- and large-object detection metrics ( $AP_M$ ,  $AP_L$ ). This indicates that the Gas Block effectively enhances long-range contextual modeling and hierarchical feature integration, thereby improving semantic consistency and robustness when detecting larger or structurally complex gas plumes. When both AGPEO and Gas Block are combined, the model achieves the highest AP of 29.5%, with  $AP_{50}$  reaching 81.0%. This demonstrates that local edge-aware feature enhancement and global physics-inspired context modeling are complementary. Their joint integration enables the backbone to capture both fine structural cues and scale-aware semantic information, leading to consistently improved detection performance across object sizes. In summary, the ablation results demonstrate that AGPEO and Gas Block each contribute substantially to detection accuracy, and their combination yields synergistic benefits. These results validate the effectiveness of the proposed Physics–Edge Hybrid Backbone in balancing local detail preservation and global contextual reasoning for infrared gas leak detection.

Table 4: Ablation experiments of the model.  $\times$  indicates the module is not used,  $\checkmark$  indicates the module is used.

Physics–Edge Hybrid Backbone	CASR-PAN	AP	$AP_{50}$	$AP_S$	$AP_M$	$AP_L$	Gflops (G)	Params (M)
$\times$	$\times$	26.8	77.8	19.9	32.0	37.1	56.9	19.873
$\checkmark$	$\times$	29.5	81.0	24.3	33.5	38.9	54.8	17.866
$\times$	$\checkmark$	29.4	79.1	23.0	<b>33.6</b>	42.2	45.8	16.939
$\checkmark$	$\checkmark$	<b>29.8</b>	<b>84.3</b>	<b>25.3</b>	32.5	<b>42.6</b>	<b>43.7</b>	<b>14.932</b>

To assess the contributions of each component in the complete PEG-DRNet, we conducted additional ablation experiments, summarized in Table 4. The baseline RT-DETR achieves an AP of 26.8%. Introducing the

Physics–Edge Hybrid Backbone increases AP to 29.5%, with consistent gains in  $AP_{50}$  (+2.7%) and  $AP_S$  (+4.4%). These improvements indicate that embedding physical priors and multi-scale edge-enhanced features strengthens low-level texture perception and structural representation, enabling more reliable detection of small-scale and boundary-sensitive gas targets. Notably, these gains are achieved alongside reduced computational cost (Gflops  $\downarrow$ 2.1, Params  $\downarrow$ 2.0M), demonstrating that the proposed backbone improves both efficiency and accuracy. Using CASR-PAN alone achieves an AP of 29.4%, reflecting its effectiveness in enhancing feature aggregation and spatial representation. This improvement stems from CASR-PAN’s content-adaptive multi-scale feature routing, which dynamically refines semantic and geometric information according to scene complexity and plume structure, leading to more robust detection performance across varying object scales. Combining both the Physics–Edge Hybrid Backbone and CASR-PAN yields the highest overall AP of 29.8% and the highest  $AP_{50}$  (84.3%). This result demonstrates the complementary nature of the two modules: the backbone emphasizes edge-aware and physics-guided feature extraction, while CASR-PAN facilitates adaptive multi-scale contextual integration. Their joint optimization improves recall and robustness, particularly under challenging conditions involving weak contrast, diffuse boundaries, and scale variability. A minor decrease in  $AP_M$  is observed when integrating the Physics–Edge Hybrid Backbone with CASR-PAN, which is mainly due to the reallocation of representational emphasis toward small-scale and large, diffuse gas regions; such scale-wise trade-offs are expected given the continuous and ambiguous nature of infrared gas plumes and do not affect the overall detection effectiveness. In conclusion, the ablation experiments confirm that the proposed modules contribute complementarily at different representation levels. The Physics–Edge Hybrid Backbone enhances edge and structural perception, whereas CASR-PAN strengthens adaptive multi-scale feature fusion. Although the overall AP remains relatively modest, this is expected in infrared gas detection due to the inherently diffuse and ambiguous boundaries of gas plumes. In such scenarios,  $AP_{50}$  serves as a more practical metric, reflecting the model’s ability to reliably detect gas regions even when precise boundary alignment is difficult. Reporting both metrics therefore provides a comprehensive evaluation, with  $AP_{50}$  emphasizing effective plume localization and AP reflecting stricter spatial accuracy.

#### 4.5. More Experiments

##### 4.5.1. Deployment Strategy Of Gas Block Across Backbone Stages

To investigate the deployment strategy of the proposed Gas Block, we adopt a physics-inspired, representation-aware design principle instead of a brute-force empirical replacement. From a feature representation perspective, lower backbone stages (P2–P3 in ResNet-18) primarily encode local textures and high-frequency details, where excessive diffusion modeling may blur discriminative structural cues. In contrast, higher-level stages (P4–P5) capture more abstract and spatially extended semantic representations, which are better aligned with the diffusion–convection characteristics of infrared gas plumes. Based on this observation, Gas Blocks are selectively introduced at P4–P5 to enhance diffusion-aware modeling while preserving low-level detail integrity and computational efficiency.

To validate this design choice, we conduct controlled ablation experiments on a ResNet-18 backbone by selectively replacing BasicBlocks with Gas Blocks at different stages, as summarized in Table 5. Replacing all BasicBlocks from P2 to P5 yields moderate improvements on  $AP_S$  (+1.2%) but degrades  $AP_M$  and  $AP_L$ , suggesting that indiscriminate diffusion modeling at early stages may interfere with hierarchical feature abstraction. In contrast, the proposed P4–P5 configuration achieves the best overall performance, with the highest AP (28.5%) and  $AP_M$  (32.8%), while maintaining a favorable balance between accuracy and efficiency. Compared to full replacement, this strategy significantly reduces computational cost (51.9 Gflops vs. 56.9 Gflops) and parameter count (16.62M vs. 19.87M), benefiting from the lightweight design of Gas Block and its selective deployment. Applying Gas Block only at P5 slightly improves  $AP_L$  but results in limited overall AP gains, indicating that single-stage high-level diffusion modeling cannot fully exploit multi-scale plume characteristics. Overall, these results empirically confirm that selective deployment of Gas Block at P4–P5 provides an effective trade-off between diffusion-aware representation, multi-scale feature learning, and computational efficiency.

##### 4.5.2. Effective Receptive Field (ERF) Analysis Of Physics–Edge Hybrid Backbone

To further verify the physical interpretability and feature propagation capability of the proposed Physics–Edge Hybrid Backbone, we conducted an effective receptive field (ERF) visualization experiment to compare it with a conventional ResNet-based backbone under identical training and inference

Table 5: Comparison of different replacement strategies of BasicBlock with Gas Block. The results demonstrate the impact of Gas Block at different backbone stages (P2–P5).

Configuration	AP	AP <sub>50</sub>	AP <sub>S</sub>	AP <sub>M</sub>	AP <sub>L</sub>	Gflops (G)	Params (M)
All BasicBlock (baseline)	26.8	77.8	19.9	32.0	37.1	56.9	19.873
P2–P5 all Gas Block	27.4	77.9	21.1	31.1	35.7	<b>47.1</b>	<b>16.421</b>
P4–P5 Gas Block, others Basic	<b>28.5</b>	<b>80.7</b>	22.2	<b>32.8</b>	37.3	51.9	16.620
P5 Gas Block, others Basic	27.0	78.6	<b>22.4</b>	30.2	<b>42.8</b>	54.5	17.267

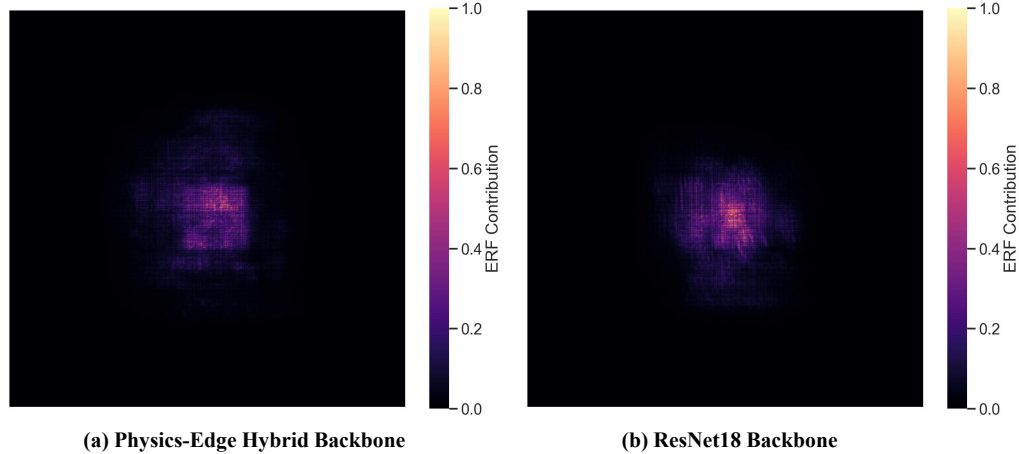


Figure 7: Effective receptive field (ERF) visualization comparison between (a) the proposed Physics–Edge Hybrid Backbone and (b) the ResNet Backbone under the same training and inference settings.

settings, as shown in Figure 7. Specifically, we employed the gradient-based ERF analysis method, where the gradient of the central activation with respect to the input pixels was accumulated and visualized as a heatmap (Ding et al., 2022). The visualization highlights high-response regions that contribute most significantly to the central neuron activation, thus reflecting the spatial extent and distribution of the model’s receptive field.

Based on the quantitative statistics of the effective receptive field (ERF) distributions, a clear difference can be observed between the proposed Physics-Edge Hybrid Backbone and the conventional ResNet backbone. As shown in Figure 8, both the bar and line plots illustrate the relationship between the high-contribution area ratio and the activation threshold. Specifically, under low thresholds (e.g., 0.2 and 0.3), Physics-Edge Hybrid Backbone already achieves slightly higher area ratios than ResNet, indicating a broader

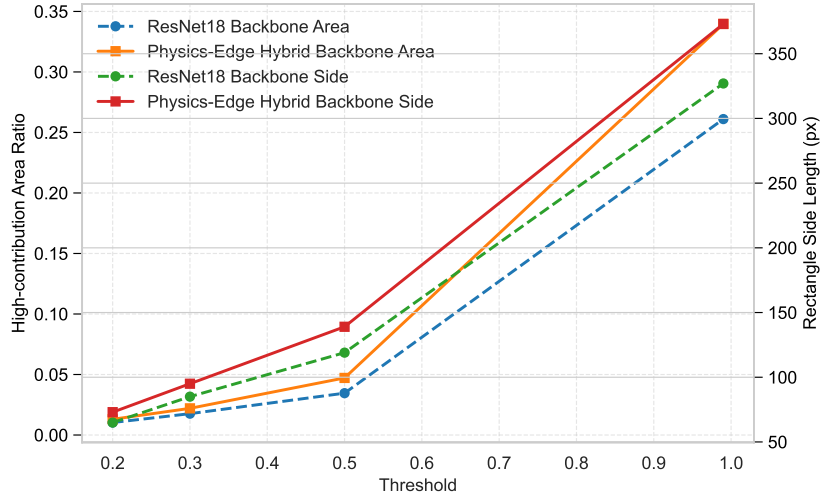


Figure 8: Comparison of high-contribution area ratios between the proposed Physics-Edge Hybrid Backbone and ResNet18 Backbone at different thresholds. The chart shows both bar values and trend lines for easy comparison.

response range even in the early activation stage. As the threshold increases to 0.5 and 0.99, this gap becomes more pronounced — the high-contribution area ratio of Gas Block reaches 0.047 and 0.340, compared with 0.036 and 0.255 for ResNet, respectively. This trend reveals that the proposed Gas Block possesses a larger and more spatially continuous receptive field, allowing information to propagate more effectively across distant regions. Consequently, the network is better able to integrate global contextual cues while preserving fine structural details, consistent with the convection–diffusion–Inspired design of Physics-Edge Hybrid Backbone.

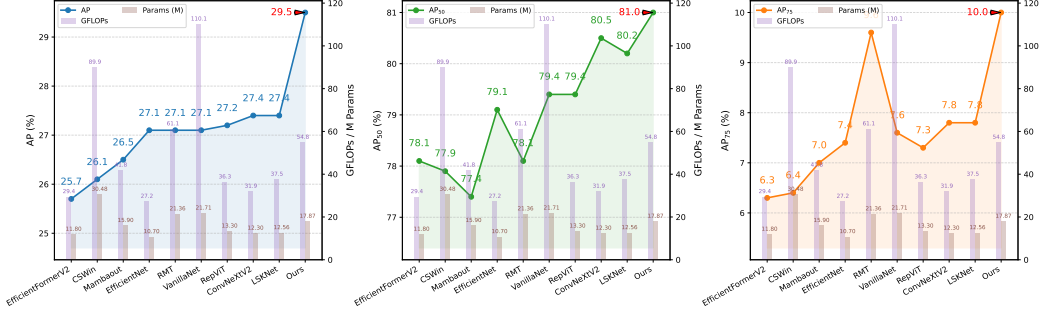


Figure 9: Performance comparison of different backbones. The red cross indicates the highest value among all models, while the red-circled point highlights the proposed Physics–Edge Hybrid Backbone. Our method achieves superior overall performance in terms of AP, AP<sub>50</sub>, and AP<sub>75</sub>.

#### 4.5.3. Backbone-Level Comparison With Representative Architectures

To comprehensively evaluate the effectiveness of the proposed Physics–Edge Hybrid Backbone, we conducted a comparative study against several representative models, including EfficientNet (Tan and Le, 2019), MambabOut (Yu and Wang, 2025), RepViT (Wang et al., 2024), CSWin Transformer (Dong et al., 2022), ConvNeXtV2 (Woo et al., 2023), RMT (Fan et al., 2024), EfficientFormerV2 (Li et al., 2023), LSKNet (Li et al., 2023), and VanillaNet (Chen et al., 2023), highlighting the performance improvements achieved by our method, as shown in Figure 9.

The results indicate that the proposed Physics–Edge Hybrid Backbone achieves the highest overall performance, obtaining an AP of 29.5%, AP<sub>50</sub> of 81.0%, and AP<sub>75</sub> of 10.0%. Compared with lightweight convolutional models such as EfficientNet and RepViT, our backbone yields approximately +2.4% AP improvement with similar parameter counts, demonstrating the superior feature extraction capability of the physics-guided diffusion–convection modeling. Moreover, compared with transformer-based architectures (e.g., CSWin and RMT), Physics–Edge Hybrid Backbone achieves higher accuracy with lower complexity, indicating better efficiency and generalization in small, faint gas plume detection scenarios.

#### 4.5.4. Visualization Analysis Of AGPEO Edge Representation

To validate the feature extraction capability of the AGPEO module, we present a comparative visualization of the original infrared image, the gradient feature map, the phase feature map, and the fused result, as shown in

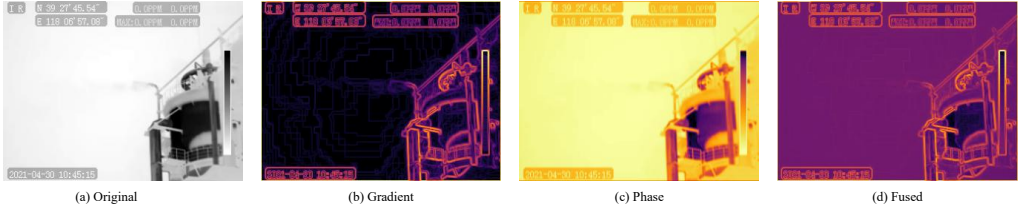


Figure 10: Visualization results of the proposed AGPEO module. (a) Original infrared image; (b) Gradient feature map extracted by directional Sobel operators; (c) Phase feature map obtained by the Gabor convolution branch; (d) Fused feature map integrating gradient and phase information.

Figure 10. It can be observed that the gradient branch, employing multi-directional Sobel operators, effectively highlights prominent edge responses, emphasizing both the gas leak regions and the structural contours of the equipment. However, due to the presence of temperature gradients and noise in the infrared image background, the gradient feature map also exhibits noticeable spurious edges in some background areas, resulting in partially fragmented boundaries. The phase branch utilizes Gabor convolutional kernels to perform local phase modulation, producing phase feature maps that are smoother in weak edge regions. This branch effectively preserves texture details while suppressing noise responses. Compared to the gradient map, the phase map shows a more uniform overall intensity distribution and stronger structural continuity. The fused feature map visually integrates the advantages of both branches: it maintains clear edge contours while also capturing fine-grained texture structures. The target regions are more prominent in the fused result, whereas background noise is significantly suppressed. These results demonstrate that the AGPEO module can effectively combine gradient and phase information, enhancing edge clarity while preserving texture stability, thereby providing more discriminative and robust feature representations for infrared gas leak detection.

#### 4.5.5. Multi-Scale Edge Representation Analysis Of MSEPM

To further investigate the edge representation capability of the proposed MSEPM, a four-scale visualization experiment was conducted, as illustrated in Figure 11. The first scale (Scale 1) corresponds to the fused edge map generated by the AGPEO module without downsampling, preserving abundant fine-grained textures and weak gas boundaries. This layer effectively delineates faint and semi-transparent gas plumes against complex infrared

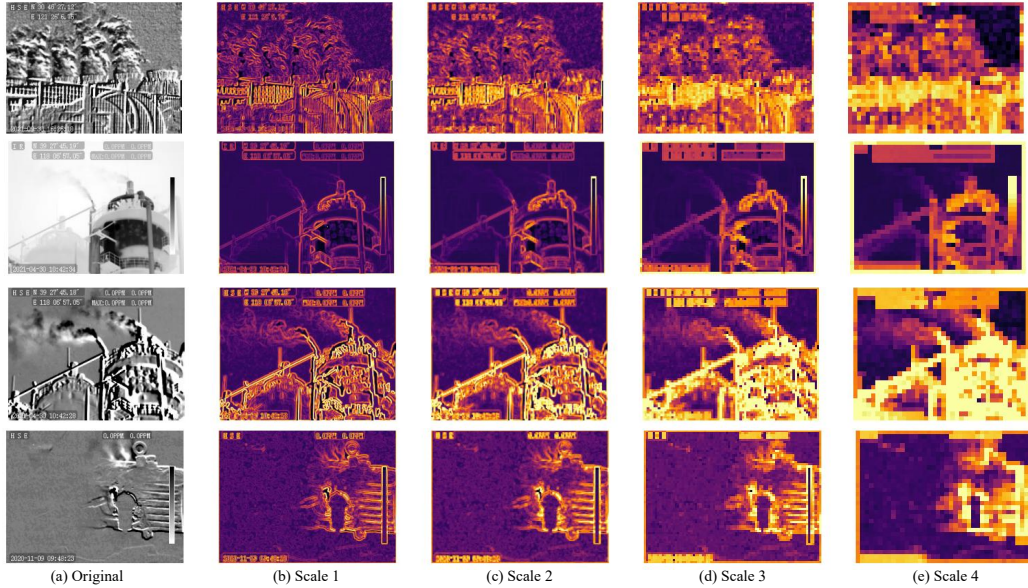


Figure 11: Visualization of multi-scale edge extraction results generated by the proposed multi-scale edge perception module. The four hierarchical outputs correspond to: (a) Original infrared image; (b) Scale 1 — shallow features at the original resolution, preserving fine-grained textures and weak gas boundaries; (c) Scale 2 — mid-shallow features after the first downsampling, suppressing local noise and enhancing contour continuity; (d) Scale 3 — mid-level features highlighting aggregated gas plume boundaries with reduced detail complexity; and (e) Scale 4 — deep features obtained after three successive pooling operations, emphasizing the global plume morphology and large-scale diffusion structures.

backgrounds. After one downsampling operation (Scale 2), local noise and minor details are moderately suppressed, while continuous contour structures begin to emerge, reflecting a balance between detail retention and edge smoothness. The third scale (Scale 3) further aggregates regional responses, enhancing the integrity of the main gas contours and emphasizing medium-scale plume boundaries. At the deepest level (Scale 4), after three successive max-pooling operations, the representation becomes dominated by the global morphology of the gas plume, highlighting large-scale diffusion structures while discarding most fine textures. Overall, the visualization clearly demonstrates that shallow scales capture detailed boundary textures of weak gas plumes, whereas deeper scales progressively abstract these responses into structural and global representations. This hierarchical perception of edge information provides complementary guidance for both fine plume localization and global morphology interpretation in infrared gas leak detection.

#### 4.5.6. Ablation On Gradient Components In AGPEO

An ablation study is conducted to analyze the impact of gradient direction modeling in the proposed AGPEO module embedded within the multi-scale edge perception module (MSEPM). AGPEO employs fixed, Sobel-like directional gradient kernels to extract orientation-sensitive edge responses, followed by phase-aware modulation. Specifically, gradients are modeled along four canonical orientations ( $0^\circ$ ,  $45^\circ$ ,  $90^\circ$ , and  $135^\circ$ ) using depthwise convolution with non-learnable directional filters, enabling efficient and stable multi-orientation gradient extraction. To examine the contribution of directional diversity, we first evaluate a degraded variant that models gradients along a single orientation ( $0^\circ$ ). We then extend the configuration to two orthogonal orientations ( $0^\circ$  and  $90^\circ$ ), and further incorporate diagonal orientations ( $45^\circ$  and  $135^\circ$ ) to investigate the effect of multi-directional gradient–phase fusion. All variants are implemented within the same MSEPM architecture, with identical downstream feature fusion and detection components. The only difference lies in the number of gradient orientations modeled in AGPEO.

Table 6: Ablation study of gradient directions in AGPEO.

Gradient Directions	AP	AP <sub>50</sub>	AP <sub>75</sub>	AP <sub>S</sub>	AP <sub>M</sub>	AP <sub>L</sub>	Gflops (G)	Params (M)
$0^\circ$	26.7	79.8	6.3	21.4	31.1	33.8	<b>59.7</b>	<b>21.117</b>
$0^\circ$ , $90^\circ$	<b>28.8</b>	<b>81.1</b>	9.4	22.1	<b>33.1</b>	<b>42.3</b>	<b>59.7</b>	21.118
$0^\circ$ , $45^\circ$ , $90^\circ$ , $135^\circ$	27.9	80.4	<b>10.3</b>	<b>24.0</b>	30.6	38.1	59.8	21.119

As shown in Table 6, all configurations are implemented within the AGPEO module embedded in the multi-scale edge perception module (MSEPM). The single-direction configuration achieves the lowest performance, particularly on AP<sub>75</sub>, indicating limited boundary localization capability due to insufficient orientation coverage. Modeling gradients along two orthogonal orientations ( $0^\circ$  and  $90^\circ$ ) leads to improved overall AP and AP<sub>50</sub>, reflecting stronger edge recall and more stable responses under coarse IoU thresholds. By further incorporating diagonal orientations ( $45^\circ$  and  $135^\circ$ ), the multi-directional configuration achieves the highest AP<sub>75</sub> and AP<sub>S</sub>, demonstrating more accurate boundary alignment and enhanced sensitivity to fine-scale and weak edge structures.

Although the overall AP and AP<sub>50</sub> slightly decrease compared to the two-direction configuration, this behavior reflects a typical precision–recall trade-off in edge modeling. Multi-directional gradients introduce richer responses

for oblique and curved edges, which may mildly affect coarse IoU-based metrics while substantially improving strict localization accuracy. These gains are achieved with negligible additional computational cost. Overall, the results confirm that multi-directional gradient–phase fusion within AGPEO is critical for high-precision edge detection.

#### 4.5.7. Effect of the Weighting Factor $\alpha$ in AGPEO

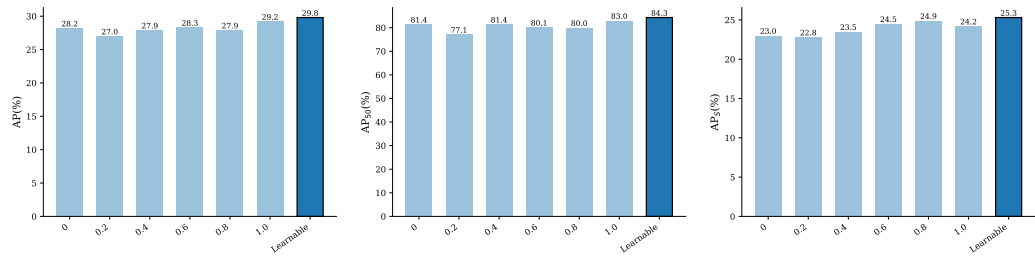


Figure 12: Effect of the fusion weight  $\alpha$  in AGPEO. Performance comparisons under  $\alpha = 0$ ,  $\alpha = 1$ , and learnable  $\alpha$  are reported in terms of (a) AP, (b) AP<sub>50</sub>, and (c) AP<sub>S</sub>.

We conduct an ablation study on the fusion weight  $\alpha$  within the AGPEO module of PEG-DRNet. Figure 12. shows the detection performance under different settings of  $\alpha$ . When  $\alpha$  is fixed, the performance varies noticeably across AP, AP<sub>50</sub>, and AP<sub>S</sub>, indicating that detection accuracy is sensitive to the choice of  $\alpha$ . Intermediate fixed values (e.g.,  $\alpha = 0.4$ – $0.8$ ) improve small-object performance, while extreme settings exhibit inconsistent behavior across metrics. The gradient-only setting ( $\alpha = 1.0$ ) achieves relatively strong overall performance, whereas the phase-only setting ( $\alpha = 0$ ) yields lower accuracy, particularly for small objects. In contrast, the learnable  $\alpha$  consistently outperforms all fixed configurations on AP, AP<sub>50</sub>, and AP<sub>S</sub>. This trend demonstrates that allowing  $\alpha$  to be optimized during training leads to more stable and effective feature fusion than manually fixing its value.

In addition to the fixed- $\alpha$  experiments, we track the evolution of the learnable fusion weight  $\alpha$  during the 200 training epochs, as shown in Figure 13. Initialized at 0.7,  $\alpha$  increases during the first  $\sim 50$  epochs and then enters a stable regime, where it remains within a narrow range of approximately 0.77–0.79 for the remainder of training. The magnitude of variation after this point is small and does not exhibit a monotonic increasing or decreasing trend, indicating practical convergence of the fusion weight. This behavior

suggests that the network consistently identifies an effective balance between gradient and phase cues, rather than drifting toward extreme gradient-only or phase-only configurations. Overall, the observed stability supports the use of a learnable fusion weight for adaptive and robust edge representation.

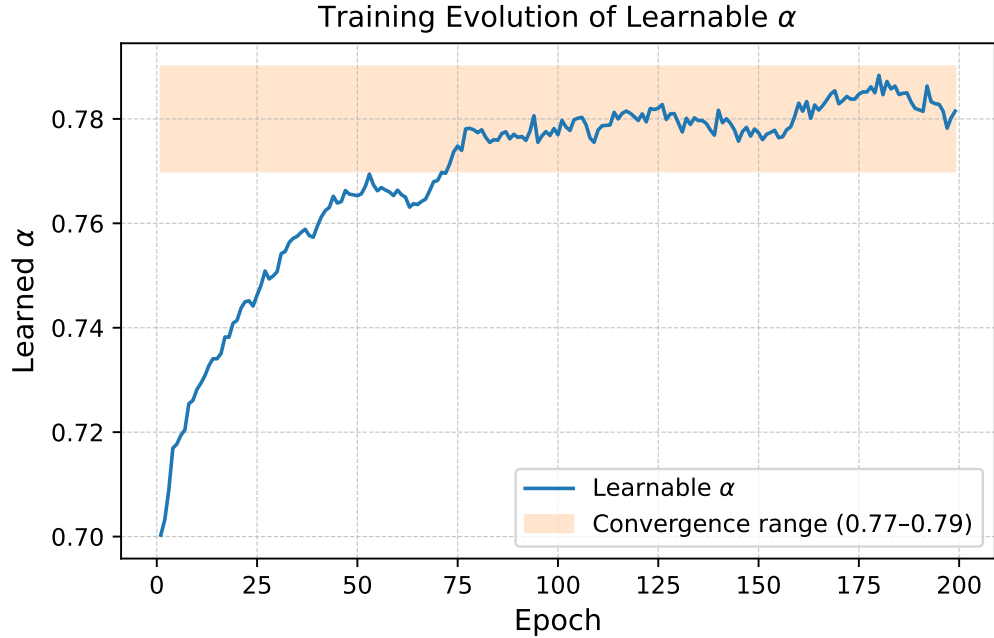


Figure 13: Training evolution of the learnable fusion weight  $\alpha$  in AGPEO during the 200 epochs. After an initial increasing phase,  $\alpha$  fluctuates within a narrow range, suggesting a stable fusion preference during training.

Table 7: Comparison of different operators.

Model	AP	AP <sub>50</sub>	AP <sub>75</sub>	AP <sub>S</sub>	AP <sub>M</sub>	AP <sub>L</sub>	Gflops (G)	Params (M)
Sobel (Heath et al., 1998)	<b>27.9</b>	79.7	8.1	21.5	32.9	33.6	<b>59.4</b>	<b>21.109</b>
Canny (Canny, 1986)	25.8	80.0	7.2	22.1	27.7	31.2	60.1	21.110
Laplacian (Wang, 2007)	26.7	79.4	8.2	21.9	30.1	29.7	59.8	21.110
AGPEO	<b>27.9</b>	<b>80.4</b>	<b>10.3</b>	<b>24.0</b>	<b>30.6</b>	<b>38.1</b>	59.8	21.119

#### 4.5.8. Comparison Of Edge Operators In MSEPM

To evaluate the effectiveness of the proposed adaptive gradient and phase edge operator (AGPEO) in edge feature extraction, we conduct a compara-

tive experiment against several classical edge detection operators, including Sobel, Canny, and Laplacian. For a fair comparison, all operators are embedded within the same multi-scale edge perception module (MSEPM), where AGPEO is replaced by each classical operator while keeping the remaining network architecture unchanged. The Sobel operator emphasizes gradient magnitude along fixed directions, which is effective for simple edges but tends to be sensitive to noise. The Canny operator introduces Gaussian smoothing and multi-threshold hysteresis to improve robustness, yet its fixed filtering mechanism limits adaptivity to complex infrared textures. The Laplacian operator captures second-order derivatives, highlighting fine edges but also amplifying high-frequency noise. In contrast, AGPEO adaptively learns multi-directional gradient responses and dynamically balances edge intensity enhancement and noise suppression through learnable parameters. This enables AGPEO to better capture high-contrast and precise edge information, leading to a significant improvement in  $AP_{75}$  (10.3% vs 8.1%/7.2%/8.2%) and  $AP_S$  (24.0% vs 21.5%/22.1%/21.9%) for small or low-contrast plumes. The slightly lower  $AP_M$  compared to Sobel (30.6% vs 32.9%) can be attributed to AGPEO’s emphasis on fine-grained details over large object coverage, reflecting a trade-off between fine edge sensitivity and global context. Overall, the quantitative results in Table 7 demonstrate that AGPEO provides superior edge representation for infrared gas plume detection, especially for small and finely structured targets.

Table 8: Ablation study on the adaptive routing mechanism in the proposed neck. Each variant removes one routing path while keeping the rest unchanged.

Model	AP	$AP_{50}$	$AP_{75}$	$AP_S$	$AP_M$	$AP_L$	Gflops (G)	Params (M)
Naive additive fusion	25.9	75.9	8.5	23.6	28.0	38.3	45.8	16.939
Without deep-to-mid fusion	27.5	79.5	7.6	22.5	31.1	36.8	45.8	16.939
Without deep-to-shallow fusion	25.7	76.2	6.8	19.2	30.5	40.6	45.8	16.939
Without shallow-to-mid fusion	25.7	75.8	6.2	19.8	29.7	40.2	45.8	16.939
Without mid-level self-fusion	28.3	<b>80.3</b>	8.3	22.3	31.9	<b>43.5</b>	45.8	16.939
CASR-PAN	<b>29.4</b>	79.1	<b>12.3</b>	<b>23.0</b>	<b>33.6</b>	42.2	<b>45.8</b>	<b>16.939</b>

#### 4.5.9. Ablation Study Of CASR-PAN Components

To evaluate the effectiveness of the proposed CASR-PAN, we conduct an ablation study focusing on its adaptive routing mechanism. All variants share the same backbone, training strategy, and computational complexity, and differ only in the feature fusion or routing design within the neck.

Table 9: Comparison of different neck structures.

Model	AP	AP <sub>50</sub>	AP <sub>75</sub>	AP <sub>S</sub>	AP <sub>M</sub>	AP <sub>L</sub>	Gflops (G)	Params (M)
PANet (Liu et al., 2018)	27.3	<b>80.9</b>	8.0	22.1	30.0	39.2	103.8	21.463
BiFPN (Tan et al., 2020)	27.0	76.6	8.3	20.8	31.3	38.9	64.3	20.300
NAS-FPN (Ghiasi et al., 2019)	25.1	76.4	7.5	19.3	29.9	26.1	93.8	19.756
CASR-PAN	<b>29.4</b>	79.1	<b>12.3</b>	<b>23.0</b>	<b>33.6</b>	<b>42.2</b>	<b>45.8</b>	<b>16.939</b>

Specifically, we compare the full CASR-PAN with a naïve additive fusion baseline and several variants in which one routing path is removed while the remaining components are kept unchanged. Performance is assessed using standard detection metrics, including AP, AP<sub>50</sub>, AP<sub>75</sub>, and scale-specific AP for small, medium, and large objects. As shown in Table 8, the naïve additive fusion baseline achieves the lowest overall performance, indicating that simple layer-wise summation is insufficient for effective multi-scale feature integration. Removing any individual routing path leads to a consistent performance degradation compared with the full CASR-PAN, demonstrating that each routing path contributes positively to detection accuracy. Among the routing paths, removing the deep-to-shallow fusion results in a notable drop in AP<sub>S</sub>, highlighting the importance of high-level semantic guidance for small-object detection. The absence of shallow-to-mid fusion mainly degrades the performance on small and medium objects, suggesting that low-level spatial details are critical for mid-level feature refinement. In contrast, removing the mid-level self-fusion primarily affects AP<sub>L</sub>, indicating its role in strengthening large-object representations. Overall, the full CASR-PAN achieves the best performance across all evaluation metrics, particularly in AP<sub>75</sub> and scale-specific AP, while maintaining identical computational cost. These results confirm that the proposed adaptive routing mechanism enables effective multi-scale feature interaction and leads to more accurate and robust detection performance.

#### 4.5.10. Comparison Of CASR-PAN With Multi-Scale Fusion Strategies

To evaluate the effectiveness of the proposed CASR-PAN for cross-scale feature aggregation, we conduct a comparative study against several representative neck architectures, including PANet (Liu et al., 2018), BiFPN (Tan et al., 2020), and NAS-FPN (Ghiasi et al., 2019). All models are integrated into the same backbone and detection head to ensure a fair comparison. The results, summarized in Table 9, demonstrate that CASR-PAN consistently outperforms other neck structures in both detection accuracy and multi-scale

feature representation, particularly for small and weakly visible gas plumes.

## 5. Conclusion

This paper presents PEG-DRNet, a single-stage infrared gas leak detector that couples physics priors with content-adaptive feature learning. The Physics–Edge Hybrid Backbone incorporates a Gas Block that emulates diffusion–convection dynamics, and an AGPEO-based multi-scale edge perception module (MSEPM) that provides robust gradient–phase edge cues for semi-transparent, weak-contrast plumes. The proposed CASR-PAN further introduces content-adaptive sparse routing via AIMM-F and AIMM-S, selectively propagating informative cross-scale features while suppressing redundancy. Experiments on the IIG infrared gas dataset and LangGas dataset show that PEG-DRNet surpasses representative CNN- and Transformer-based detectors, achieving consistent improvements in  $AP$ ,  $AP_{50}$ , and  $AP_S$  over RT-DETR, while maintaining a lightweight design with 43.7 Gflops and 14.93M parameters, making it suitable for real-time deployment. Ablation studies confirm the complementary roles of physics priors, edge-guided enhancement, and adaptive routing. Future work will extend this framework toward temporal–spectral gas diffusion modeling, multi-gas joint detection, and edge-intelligent deployment in industrial monitoring scenarios. In addition, recent advances in vision foundation models and large-scale multimodal models have demonstrated remarkable generalization capabilities under limited or even zero-shot supervision. Exploring how such foundation models can be effectively adapted or distilled for infrared gas leak detection—particularly to alleviate data scarcity and improve robustness across unseen environments—represents a promising direction for future research.

## 6. CRediT Authorship Contribution Statement

Dongsheng Li: Conceptualization, Data curation, Formal analysis, Investigation, Methodology, Software, Validation, Visualization, Writing – original draft, Writing – review & editing. Tianli Ma: Funding acquisition, Supervision. Siling Wang: Software, Validation, Visualization, Writing – original draft. Beibei Duan: Validation, Supervision. Song Gao: Funding acquisition, Supervision, Writing – review & editing.

## 7. Data Availability

Data will be made available on request.

## 8. Funding

This work was supported in part by the National Natural Science Foundation of China (No. 62303368), by the National Foreign Experts Project (No. H20251091), by the Qin Chuang Yuan “Scientist + Engineer” Team Construction Project (No. 2024QCY-KXJ-172).

## 9. List of Abbreviations

Table 10: List of abbreviations used in this paper

Abbreviation	Meaning
RT-DETR	real-time detection transformer
PEG-DRNet	physics-edge hybrid gas dynamic routing network
AGPEO	adaptive gradient and phase edge operator
MSEPM	multi-scale edge perception module
CASR-PAN	content-adaptive sparse routing path aggregation network
AIMM-F	adaptive information modulation module-fusion
AIMM-S	adaptive information modulation module-self
FPN	feature pyramid network
PANet	path aggregation network
BiFPN	bi-directional feature pyramid network
BA	bias addition
IDAS	identity-aware scaling
IE	importance estimator
DCT	discrete cosine transform
IDCT	inverse discrete cosine transform
AIFI	attention-based intra-scale feature interaction

## References

Bonvicini, S., Antonioni, G., Morra, P., & Cozzani, V. (2015). Quantitative assessment of environmental risk due to accidental spills from on-shore pipelines. *Process Safety and Environmental Protection*, 93, 31–49.<https://doi.org/10.1016/j.psep.2014.04.007>.

Canny, J. (1986). A computational approach to edge detection. *IEEE Transactions on Pattern Analysis and Machine Intelligence*, 8, 679–698.<https://doi.org/10.1109/TPAMI.1986.4767851>.

Carion, N., Massa, F., Synnaeve, G., Usunier, N., Kirillov, A., & Zagoruyko, S. (2020). End-to-end object detection with transformers. In *European Conference on Computer Vision* (pp. 213–229). Springer.[https://doi.org/10.1007/978-3-030-58452-8\\_13](https://doi.org/10.1007/978-3-030-58452-8_13).

Chen, H., Wang, Y., Guo, J., & Tao, D. (2023). VanillaNet: The power of minimalism in deep learning. *Advances in Neural Information Processing Systems*, 36, (pp. 7050–7064).

Chen, X., Li, X., Fu, B., Hou, X., Gan, W., & Huang, C. (2024). FBG strain sensing technology-based gas pipeline leak monitoring and accurate location. *Engineering Failure Analysis*, 159, 108102.<https://doi.org/10.1016/j.engfailanal.2024.108102>.

Ding, X., Zhang, X., Han, J., & Ding, G. (2022). Scaling up your kernels to  $31 \times 31$ : Revisiting large kernel design in CNNs. In *2022 IEEE/CVF Conference on Computer Vision and Pattern Recognition (CVPR)* (pp. 11953–11965).<https://doi.org/10.1109/CVPR52688.2022.01166>.

Dong, X., Bao, J., Chen, D., Zhang, W., Yu, N., Yuan, L., Chen, D., & Guo, B. (2022). CSWin Transformer: A general vision transformer backbone with cross-shaped windows. In *2022 IEEE/CVF Conference on Computer Vision and Pattern Recognition (CVPR)* (pp. 12114–12124).<https://doi.org/10.1109/CVPR52688.2022.01181>.

Fan, Q., Huang, H., Chen, M., Liu, H., & He, R. (2024). RMT: Retentive Networks Meet Vision Transformers. In *2024 IEEE/CVF Conference on Computer Vision and Pattern Recognition (CVPR)* (pp. 5641–5651).<https://doi.org/10.1109/CVPR52733.2024.00539>.

Girshick, R., Donahue, J., Darrell, T., & Malik, J. (2014). Rich feature hierarchies for accurate object detection and semantic segmentation. In *2014 IEEE Conference on Computer Vision and Pattern Recognition (CVPR)* (pp. 580–587).<https://doi.org/10.1109/CVPR.2014.81>.

Girshick, R. (2015). Fast R-CNN. In *2015 IEEE International Conference on Computer Vision (ICCV)* (pp. 1440–1448).<https://doi.org/10.1109/ICCV.2015.169>.

Ghiasi, G., Lin, T.-Y., & Le, Q. V. (2019). NAS-FPN: Learning Scalable Feature Pyramid Architecture for Object Detection. In *2019 IEEE/CVF Conference on Computer Vision and Pattern Recognition (CVPR)* (pp. 7029–7038).<https://doi.org/10.1109/CVPR.2019.00720>.

[dataset]Guo, W. M., & Du, Y. (2025). LangGas: Introducing language in selective zero-shot background subtraction for semi-transparent gas leak detection with a new dataset. In *2025 IEEE/CVF Conference on Computer Vision and Pattern Recognition Workshops (CVPRW)* (pp. 4490–4500).<https://doi.org/10.1109/CVPRW67362.2025.00434>.

Heath, M., Sarkar, S., Sanocki, T., & Bowyer, K. (1998). Comparison of edge detectors: A methodology and initial study. *Computer Vision and Image Understanding*, 69, 38–54.<https://doi.org/10.1006/cviu.1997.0587>.

Han, Y., Feng, X., & Todd, M. D. (2023). A novel methodology for quantitative identification of pipeline leakage and negative pressure wave velocity. *Structural Health Monitoring*, 22, 2267–2279.<https://doi.org/10.1177/14759217221123403>.

Jiang, P., Ergu, D., Liu, F., Cai, Y., & Ma, B. (2022). A review of YOLO algorithm developments. *Procedia Computer Science*, 199, 1066–1073.<https://doi.org/10.1016/j.procs.2022.01.135>.

Jing, Y., Sun, Y., & Wang, Q. (2025). Lightweight single-stage network for gas leak detection based on infrared imaging. *IEEE Transactions on Instrumentation and Measurement*, 7, 1–9.<https://doi.org/10.1109/TIM.2025.3561424>.

Kopbayev, A., Khan, F., Yang, M., & Halim, S. Z. (2022). Gas leakage detection using spatial and temporal neural network model. *Process Safety and Environmental Protection*, 160, 968–975.<https://doi.org/10.1016/j.psep.2022.03.002>.

Kang, Z., Qian, X., Li, Y., Hou, L., Huang, Z., Duanmu, W., & Yuan, M. (2023). Feature extraction of natural gas leakage for an intelligent warning model: A data-driven analysis and

modeling. *Process Safety and Environmental Protection*, 174, 574–584.<https://doi.org/10.1016/j.psep.2023.04.026>.

Khanam, R., & Hussain, M. (2024). YOLOv11: An overview of the key architectural enhancements. *arXiv preprint arXiv:2410.17725*.<https://arxiv.org/abs/2410.17725>.

Lin, T.-Y., Maire, M., Belongie, S., Hays, J., Perona, P., Ramanan, D., Dollár, P., & Zitnick, C. L. (2014). Microsoft COCO: Common objects in context. In *European Conference on Computer Vision* (pp. 740–755). Springer.[https://doi.org/10.1007/978-3-319-10602-1\\_48](https://doi.org/10.1007/978-3-319-10602-1_48).

Liu, W., Anguelov, D., Erhan, D., Szegedy, C., Reed, S., Fu, C.-Y., & Berg, A. C. (2016). SSD: Single shot multibox detector. In *European Conference on Computer Vision* (pp. 21–37).[https://doi.org/10.1007/978-3-319-46448-0\\_2](https://doi.org/10.1007/978-3-319-46448-0_2).

Lin, T.-Y., Dollár, P., Girshick, R., He, K., Hariharan, B., & Belongie, S. (2017). Feature pyramid networks for object detection. In *2017 IEEE Conference on Computer Vision and Pattern Recognition (CVPR)* (pp. 936–944).<https://doi.org/10.1109/CVPR.2017.106>.

Liu, S., Qi, L., Qin, H., Shi, J., & Jia, J. (2018, June). Path aggregation network for instance segmentation. In *2018 IEEE/CVF Conference on Computer Vision and Pattern Recognition (CVPR)* (pp. 8759–8768).<https://doi.org/10.1109/CVPR.2018.00913>.

Lu, H., Iseley, T., Behbahani, S., & Fu, L. (2020). Leakage detection techniques for oil and gas pipelines: State-of-the-art. *Tunnelling and Underground Space Technology*, 98, 103249.<https://doi.org/10.1016/j.tust.2019.103249>.

Li, F., Zhang, H., Liu, S., Guo, J., Ni, L. M., & Zhang, L. (2022). DN-DETR: Accelerate DETR Training by Introducing Query DeNoising. In *2022 IEEE/CVF Conference on Computer Vision and Pattern Recognition (CVPR)* (pp. 13609–13617).<https://doi.org/10.1109/CVPR52688.2022.01325>.

Li, Y., Hou, Q., Zheng, Z., Cheng, M.-M., Yang, J., & Li, X. (2023). Large selective kernel network for remote sensing object detection. In *2023*

*IEEE/CVF International Conference on Computer Vision (ICCV)* (pp. 16748–16759).<https://doi.org/10.1109/ICCV51070.2023.01540>.

Li, Y., Hu, J., Wen, Y., Evangelidis, G., Salahi, K., Wang, Y., Tulyakov, S., & Ren, J. (2023). Rethinking vision transformers for MobileNet size and speed. In *2023 IEEE/CVF International Conference on Computer Vision (ICCV)* (pp. 16843–16854).<https://doi.org/10.1109/ICCV51070.2023.01549>.

Li, H., Zhang, R., Pan, Y., Ren, J., & Shen, F. (2024). LR-FPN: Enhancing remote sensing object detection with location refined feature pyramid network. In *2024 International Joint Conference on Neural Networks (IJCNN)* (pp. 1–8).<https://doi.org/10.1109/IJCNN60899.2024.10650583>.

Li, K., Chen, W., Zou, Y., Wang, Z., Zhou, X., & Shi, J. (2025). Optimized PSOMV-VMD combined with ConvFormer model: A novel gas pipeline leakage detection method based on low sensitivity acoustic signals. *Measurement*, 247, 116804.<https://doi.org/10.1016/j.measurement.2025.116804>.

Li, J., Lu, Y., Guo, X., Xian, X., Wang, T., & Shi, Y. (2026). Exploiting Gaussian agnostic representation learning with diffusion priors for enhanced infrared small target detection. *Neural Networks*, 194, 108185.<https://doi.org/10.1016/j.neunet.2025.108185>.

Meng, D., Chen, X., Fan, Z., Zeng, G., Li, H., Yuan, Y., Sun, L., & Wang, J. (2021). Conditional DETR for Fast Training Convergence. In *2021 IEEE/CVF International Conference on Computer Vision (ICCV)* (pp. 3631–3640).<https://doi.org/10.1109/ICCV48922.2021.00363>.

Meribout, M. (2021). Gas leak-detection and measurement systems: Prospects and future trends. *IEEE Transactions on Instrumentation and Measurement*, 70, 1–13.<https://doi.org/10.1109/TIM.2021.3096596>.

Pan, J., Peng, D., Wang, D., Zhao, H., & Qu, B. (2025). SRHS-Net: A hybrid attentive architecture for real-time steam leak detection in power plants. *IEEE Transactions on Industrial Informatics*, 21(9), 6879–6890.<https://doi.org/10.1109/TII.2025.3568498>.

Quy, T. B., & Kim, J.-M. (2022). Pipeline leak detection using acoustic emission and state estimate in feature space.

*IEEE Transactions on Instrumentation and Measurement*, 71, 1–9.<https://doi.org/10.1109/TIM.2022.3206833>.

Qiao, C., Shen, F., Wang, X., Wang, R., Cao, F., Zhao, S., & Li, C. (2022). A novel multi-frequency coordinated module for SAR ship detection. In *2022 IEEE 34th International Conference on Tools with Artificial Intelligence (ICTAI)* (pp. 804–811).<https://doi.org/10.1109/ICTAI56018.2022.00124>.

Ren, S., He, K., Girshick, R., & Sun, J. (2017). Faster R-CNN: Towards real-time object detection with region proposal networks. *IEEE Transactions on Pattern Analysis and Machine Intelligence*, 39, 1137–1149.<https://doi.org/10.1109/TPAMI.2016.2577031>.

Strahl, T., Herbst, J., Lambrecht, A., Maier, E., Steinebrunner, J., & Wöllensteini, J. (2021). Methane leak detection by tunable laser spectroscopy and mid-infrared imaging. *Applied Optics*, 60, C68–C75.<https://doi.org/10.1364/AO.419942>.

Shen, F., & Tang, J. (2024). ImagPose: A unified conditional framework for pose-guided person generation. *Advances in Neural Information Processing Systems*, 37, 6246–6266.

Shen, F., Ye, H., Zhang, J., Wang, C., Han, X., & Wei, Y. (2024). Advancing pose-guided image synthesis with progressive conditional diffusion models. In *Proceedings of the Twelfth International Conference on Learning Representations*.

Shen, F., Xu, W., Yan, R., Zhang, D., Shu, X., & Tang, J. (2025). IMAGEDit: Let any subject transform. *arXiv preprint arXiv:2510.01186*.<https://arxiv.org/abs/2510.01186>.

Shen, F., Jiang, X., He, X., Ye, H., Wang, C., Du, X., Li, Z., & Tang, J. (2025). Imagdressing-v1: Customizable virtual dressing. In *Proceedings of the AAAI Conference on Artificial Intelligence*, 39, 6795–6804.<https://doi.org/10.1609/aaai.v39i7.32729>.

Shen, F., Ye, H., Liu, S., Zhang, J., Wang, C., Han, X., & Wei, Y. (2025). Boosting consistency in story visualization with rich-contextual conditional diffusion models. In *Proceedings of the AAAI Conference on Artificial Intelligence*, 39, 6785–6794.<https://doi.org/10.1609/aaai.v39i7.32728>.

Shen, F., Du, X., Gao, Y., Yu, J., Cao, Y., Lei, X., & Tang, J. (2025). IMAGHarmony: Controllable image editing with consistent object quantity and layout. *arXiv preprint arXiv:2506.01949*.<https://arxiv.org/abs/2506.01949>.

Shen, F., Yu, J., Wang, C., Jiang, X., Du, X., & Tang, J. (2025). IMAGGarment-1: Fine-grained garment generation for controllable fashion design. *arXiv preprint arXiv:2504.13176*.<https://arxiv.org/abs/2504.13176>.

Tan, M., & Le, Q. (2019). EfficientNet: Rethinking model scaling for convolutional neural networks. In K. Chaudhuri & R. Salakhutdinov (Eds.), *Proceedings of the 36th International Conference on Machine Learning* (pp. 6105–6114).

Tan, M., Pang, R., & Le, Q. V. (2020). EfficientDet: Scalable and efficient object detection. In *Proceedings of the 2020 IEEE/CVF Conference on Computer Vision and Pattern Recognition (CVPR)* (pp. 10778–10787).<https://doi.org/10.1109/CVPR42600.2020.01079>.

Tian, Y., Ye, Q., & Doermann, D. (2025). YOLOv12: Attention-centric real-time object detectors. *arXiv preprint arXiv:2502.12524*.<https://doi.org/10.48550/arXiv.2502.12524>.

Vergara, A., Vembu, S., Ayhan, T., Ryan, M. A., Homer, M. L., & Huerta, R. (2012). Chemical gas sensor drift compensation using classifier ensembles. *Sensors and Actuators B: Chemical*, 166, 320–329.<https://doi.org/10.1016/j.snb.2012.01.074>.

Wang, X. (2007). Laplacian operator-based edge detectors. *IEEE Transactions on Pattern Analysis and Machine Intelligence*, 29, 886–890.<https://doi.org/10.1109/TPAMI.2007.1027>.

Wang, J., Tchapmi, L. P., Ravikumar, A. P., McGuire, M., Bell, C. S., Zimmerle, D., Savarese, S., & Brandt, A. R. (2020). Machine vision for natural gas methane emissions detection using an infrared camera. *Applied Energy*, 257, 113998.<https://doi.org/10.1016/j.apenergy.2019.113998>.

Wang, J., Ji, J., Ravikumar, A. P., Savarese, S., & Brandt, A. R. (2022). VideoGasNet: Deep learning for natural gas

methane leak classification using an infrared camera. *Energy*, 238, 121516.<https://doi.org/10.1016/j.energy.2021.121516>.

Wang, L., Cheng, Y., Gopalan, S., Luo, F., Amreen, K., Singh, R. K., Goel, S., Lin, Z., & Naidu, R. (2023). Review and perspective: Gas separation and discrimination technologies for current gas sensors in environmental applications. *ACS Sensors*, 8, 1373–1390.<https://doi.org/10.1021/acssensors.2c02810>.

Woo, S., Debnath, S., Hu, R., Chen, X., Liu, Z., Kweon, I. S., & Xie, S. (2023). ConvNeXt V2: Co-designing and scaling ConvNets with masked autoencoders. In *2023 IEEE/CVF Conference on Computer Vision and Pattern Recognition (CVPR)* (pp. 16133–16142).<https://doi.org/10.1109/CVPR52729.2023.01548>.

Wang, A., Chen, H., Liu, L., Chen, K., Lin, Z., Han, J., & others. (2024). Yolov10: Real-time end-to-end object detection. *Advances in Neural Information Processing Systems*, 37, 107984–108011.

Wang, A., Chen, H., Lin, Z., Han, J., & Ding, G. (2024). Rep ViT: Revisiting Mobile CNN From ViT Perspective. In *2024 IEEE/CVF Conference on Computer Vision and Pattern Recognition (CVPR)* (pp. 15909–15920).<https://doi.org/10.1109/CVPR52733.2024.01506>.

Weng, W., Wei, M., Ren, J., & Shen, F. (2024). Enhancing aerial object detection with selective frequency interaction network. *IEEE Transactions on Artificial Intelligence*, 5(12), 6109–6120.<https://doi.org/10.1109/TAI.2024.3381096>.

Wang, F., Zhao, H., Peng, Y., Fang, J., Liu, P., & Zhang, R. (2026). MIGAN: Mambas make strong GAN for infrared image generation. *Neural Networks*, 193, 108021.<https://doi.org/10.1016/j.neunet.2025.108021>.

Xu, G., Chen, Y., Yang, M., Li, S., & Marma, K. J. S. (2023). An outlook analysis on China's natural gas consumption forecast by 2035: Applying a seasonal forecasting method. *Energy*, 284, 128602.<https://doi.org/10.1016/j.energy.2023.128602>.

[dataset] Yu, H., Wang, J., Wang, Z., Yang, J., Huang, K., Lu, G., Deng, F., & Zhou, Y. (2024). A lightweight network based on

local-global feature fusion for real-time industrial invisible gas detection with infrared thermography. *Applied Soft Computing*, 152, 111138.<https://doi.org/10.1016/j.asoc.2023.111138>.

Yao, J., Xiong, Z., Li, S., Yu, Z., & Liu, Y. (2024). TSFF-Net: A novel lightweight network for video real-time detection of SF<sub>6</sub> gas leaks. *Expert Systems with Applications*, 247, 123219.<https://doi.org/10.1016/j.eswa.2024.123219>.

Yao, L., Zhang, L., Wang, L., Li, R., & Luo, H. (2025). A spatiotemporal data-driven framework for acoustic signal-based natural gas pipeline leak detection. *IEEE Transactions on Instrumentation and Measurement*, 74, 1–12.<https://doi.org/10.1109/TIM.2025.3556201>.

Yu, W., & Wang, X. (2025). MambaOut: Do we really need Mamba for vision? In *2025 IEEE/CVF Conference on Computer Vision and Pattern Recognition (CVPR)* (pp. 4484–4496).<https://doi.org/10.1109/CVPR52734.2025.00423>.

Zimmerle, D., Vaughn, T., Bell, C., Bennett, K., Deshmukh, P., & Thoma, E. (2020). Detection limits of optical gas imaging for natural gas leak detection in realistic controlled conditions. *Environmental Science & Technology*, 54, 11506–11514.<https://doi.org/10.1021/acs.est.0c01285>.

Zhao, L., Cao, Z., & Deng, J. (2024). A review of leak detection methods based on pressure waves in gas pipelines. *Measurement*, 236, 115062.<https://doi.org/10.1016/j.measurement.2024.115062>.

Zhong, S., Zhou, H., Zheng, Z., Ma, Z., Zhang, F., & Duan, J. (2024). Hierarchical attention-guided multiscale aggregation network for infrared small target detection. *Neural Networks*, 171, 485–496.<https://doi.org/10.1016/j.neunet.2023.12.036>.

Zhao, Y., Lv, W., Xu, S., Wei, J., Wang, G., Dang, Q., Liu, Y., & Chen, J. (2024). DETRs beat YOLOs on real-time object detection. In *2024 IEEE/CVF Conference on Computer Vision and Pattern Recognition (CVPR)* (pp. 16965–16974).<https://doi.org/10.1109/CVPR52733.2024.01605>.

Zuo, Z., Zhang, H., Ma, L., Liu, T., & Liang, S. (2024). Leak detection for natural gas gathering pipelines under multiple operating conditions using RP-1dConvLSTM-AE and multi-model decision. *IEEE Transactions on Industrial Electronics*, 71, 6263–6273. <https://doi.org/10.1109/TIE.2023.3294645>.

Zhang, F., Hu, H., Zou, B., & Luo, M. (2025). M4Net: Multi-level multi-patch multi-receptive multi-dimensional attention network for infrared small target detection. *Neural Networks*, 183, 107026. <https://doi.org/10.1016/j.neunet.2024.107026>.